EXPERIMENTS ON MODE COMPETITION IN TEMPORALLY-MODULATED TAYLOR-COUETTE FLOW

by

Michael Joseph Belisle

A Thesis Presented in Partial Fulfillment
of the Requirements for the Degree
Master of Science

ARIZONA STATE UNIVERSITY

December 2007

EXPERIMENTS ON MODE COMPETITION
IN TEMPORALLY-MODULATED TAYLOR-COUETTE FLOW

by

Michael Joseph Belisle

has been approved

August 2007

Graduate Supervisory Committee:

William S. Saric, Co-Chair
Juan M. Lopez, Co-Chair
Ronald J. Adrian

ACCEPTED BY THE GRADUATE COLLEGE

ABSTRACT

Experiments are performed in Taylor-Couette flow where the inner-cylinder angular velocity is modulated in time about zero mean. Theory and nonlinear computations have previously found this case to be characterized by two competing modes. Both are axisymmetric and synchronous with the modulation, but have different spatio-temporal symmetries and axial wavenumbers.

The results of flow-visualization using reflective flakes provide the first experimental evidence and characterization of both modes. Excellent verification of the dynamical behavior for forcing Reynolds amplitudes greater than 200 is demonstrated. A region of competition is found coincident with an expected coexistence region where both modes are stable; however, the experimental flow in this region is unsteady with time-varying wavenumber.

Experimental noise limits the breadth of the results and only Reynolds amplitude of 240 is considered in detail. Lower amplitudes are also considered, but noise effects dominate as the amplitude approaches the critical around 110.

ACKNOWLEDGMENTS

I must acknowledge the relentless support and direction provided by my co-advisors, Profs. William S. Saric and Juan M. Lopez. The computational data for comparison are primarily attributable to Mr. Marc Àvila, who offered valuable insights throughout the course of study. The practical guidance of Mr. Danny Clevenger was of great utility in the technical aspects of experimentation. I would also like to thank my parents, Gary and Marcia Belisle, for their understanding and encouragement.

TABLE OF CONTENTS

Page

LIST OF FIGURES . . . vii

LIST OF NOMENCLATURE . . . ix

CHAPTER

1 INTRODUCTION . . . 1
  1.1 Stability of steady Taylor-Couette flow . . . 1
  1.2 Modulated Taylor-Couette flow . . . 5
    1.2.1 Stable modes in zero-mean modulated flow . . . 7
  1.3 Experimental considerations . . . 10

2 EXPERIMENTAL APPARATUS . . . 12

3 EXPERIMENTAL METHOD . . . 16
  3.1 Motion control . . . 16
  3.2 Data acquisition . . . 17
    3.2.1 Motion . . . 17
    3.2.2 Temperature . . . 18
  3.3 Image acquisition . . . 18
    3.3.1 Visualization using reflective flakes . . . 18
    3.3.2 Construction of space-time diagrams . . . 20
    3.3.3 Determination of the wavenumber . . . 20
    3.3.4 Determination of traveling wave frequency . . . 21

4 RESULTS AND DISCUSSION . . . 22
  4.1 Transition to to mode B . . . 22
  4.2 Temperature dependence . . . 24
  4.3 Modes A & B . . . 25
  4.4 Transition from one mode to the other . . . 27
  4.5 Time scales . . . 29

5 CONCLUSIONS . . . 31

REFERENCES CITED . . . 33

APPENDIX

A APPARATUS VERIFICATION 35

A.1 Alignment 36

A.2 Temperature and viscosity 36

A.3 Modulation 37

A.4 Critical Reynold's number for the first birfucation in the steady case 39

A.5 Length measurement 41

A.6 Vibration and roughness 41

LIST OF FIGURES

Figure Page

1.1 Problem geometry in steady case, showing velocity profile of subcritical flow. 2

1.2 (*a*) Streamlines and (*b*) angular moment countours of Taylor-Vortex flow just about Re_c^0. 4

1.3 Wave number dependence on *Re* and the Eckhaus instability. 5

1.4 Results of Floquet analysis from Avila *et al.* (2007). The solid circle denotes the bicritical point $(\omega, Re_{a,c}) = (3.936, 119.4)$. 8

1.5 Stability regions for stable modes. Solid lines are from Floquet analysis above; dashed lines are from nonlinear computations (from Avila *et al.* 2007). 8

1.6 Angular momentum (rv_θ) and azimuthal vorticity (ω_θ) contours of mode B (from Avila *et al.* 2007). 9

1.7 Angular momentum (rv_θ) and azimuthal vorticity (ω_θ) contours of mode A (from Avila *et al.* 2007). 10

2.1 Diagram of experimental apparatus. 13

2.2 Photo of experimental apparatus. 14

3.1 Discretized sine wave used in motion control. 17

3.2 Image post-processing flow chart. 19

4.1 (*a*) Time history at $Re_a = 92$, $\omega = 6.1$ showing subcritical vortex structure that grows and decays in each period. (*b*) standard deviation compared to Reynolds number and angular acceleration. 22

4.2 Time history at $Re_a = 120$, $\omega = 6.1$ showing front between noise-sustained vortices below $z \approx 17$ and mode B above. 23

4.3 Time history at $Re_a = 140$, $\omega = 6.1$, showing a traveling wave with frequency $f \approx 0.06$. 23

4.4 Frequency of traveling wave versus *Re* for $\omega = 6$. 24

4.5 (*a*) Direction of fluid motion for stationary cylinders subject to a postive radial temperature gradient; (*b*) leftward spiral; and (*c*) rightward spiral (adapted from Deters & Egbers 2005). 24

Figure Page

4.6 Data at $Re_a = 120$, $\omega = 2.5$ showing the change in behavior with the sign of the radial temperature gradient: (*a*) time history; (*b*) highlighted inflow jets and markings to illustrate spiral direction; *b* temperature of air inside test section chamber. 25

4.7 Data at $Re_a = 240$, $\omega = 1.0$ showing the change in behavior with the sign of the radial temperature gradient: (*a*) $dT \approx 0$, $k \in 2.8$; (*b*) $dT > 0$, $k \in 3.8$. 26

4.8 Space-time diagrams, normalized standard deviation σ^2, and kinetic energy KE at $Re_a = 240$: (*a*) mode A at $\omega = 1.0$, $k = 3.0$ and (*b*) mode B at $\omega = 6.1$, $k = 3.4$. 26

4.9 Diagram of observed behaviors at $Re = 240$. ● corresponds to observed stable wave numbers, while $\bigtriangledown$ and $\bigtriangleup$ respectively represent the overall maxima and minima of unsteady wavenumbers over all runs. The range of the coexistence region as computed by the nonlinear computations (Avila *et al.* 2007) is shown on the abscissa. 28

4.10 Observed ranges of unsteady wave numbers in the competition region. 29

4.11 Typical wave number variation for $Re_a = 240$, $\omega = 2.0$. 29

4.12 Representative example of a flow settling on a uniform and steady wavenumber. Conditions are $Re = 240$, $\omega = 1.0$. 30

A.1 Typical temperature variation over 30 forcing periods at $\omega = 5.1$. 37

A.2 Error in generated sine wave from a pure sine wave as measured by the encoder. 38

A.3 Standard deviation plotted for ramping Re^0 to determine Re^0_c. 40

A.4 Standard deviation plotted for ramping Re^0 to determine Re^0_c. 40

LIST OF NOMENCLATURE

$\bar{k}$	Mean wavenumber of a series of wavenumber measurements
ν	kinematic viscosity of working fluid
d	gap width, $r_o - r_i$
f	Traveling wave frequency
h	length of test section
I	Reflected intensity of a pixel in $[0, 1]$
k, k_c	axial wavenumber, $2\pi d/\lambda$; critical wavenumber
r, θ, z	coordinates of cylindrical system normalized by d
r_i, r_o	radii of inner and outer cylinders
Re	Instantaneous Reynold's number, $\Omega_i r_i d/\nu$
Re^0	Reynold's number in unmodulated case, $\Omega^0 r_i d/\nu$
Re_a	Maximum forcing Reynold's number, $\Omega_a r_i d/\nu$
Re_c^0	Critical Reynolds number in steady case, $\Omega_c^0 r_i d/\nu$
$Re_{a,c}$	Critical modulated Reynolds number, $\Omega_{a,c} r_i d/\nu$
t	Dimensionless time normalized by d^2/ν
v_r, v_θ, v_z	radial, axial, and azimuthal velocities normalized by ν/d
η	radius ratio, r_i/r_o
Γ	aspect ratio of apparatus, h/d
λ	axial vortex pair wavelength
Ω	fluid angular velocity
ω	Forcing frequency
ω_θ	Azimuthal vorticity
Ω_c^0	critical angular velocity in steady case
Ω_i, Ω_o	inner and outer cylinder angular velocities
σ_I	Standard deviation of measured light intensity
σ_k	Standard deviation of a series of wave number measurements

CHAPTER 1

INTRODUCTION

Situations involving transition from one state to another are ubiquitous in nature. In fluid mechanics, the transition that has attracted the most interest and study is that of a flow from a laminar state to a turbulent state. This laminar–turbulent transition is a complex and challenging problems and remains one of the great unsolved problems in fluid mechanics. It is of great utility to study simpler problems where a progression of instabilities leads to flow states that preserve the dynamics of interest. This progression is often of increasing spatial and temporal complexity.

One such problem is the study of flow in the annulus of two concentric cylinders. This class of problems is known as Taylor-Couette flow, after the two pioneering researchers in the field, Taylor (1923) and Couette (1890). Although the problem has relatively simple boundary conditions, a myriad of stable states are possible in the diverse parameter space.

In the simplest case, the inner cylinder is rotated steadily about its longitudinal axis. The basic flow, Circular Couette (CC) flow, is stable and symmetric independent of both the axial and azimuthal directions (in the idealized limit of an infinitely long annulus).

Rotating the inner cylinder is just one of many possible parameters. Among the other parameters that have attracted significant interest include rotating the outer cylinder introducing an axial flow, applying a radial temperature gradient, and adding spatial variation to the system (e.g. a ramp or spherical geometry). In addition, any of these parameters can be modulated or varied in time. This thesis considers experiments in the relatively simple case where the rotation of the inner cylinder is modulated in time about a zero mean—like the agitator in a washing machine.

1.1. Stability of steady Taylor-Couette flow

When the inner cylinder is rotated at constant angular speed Ω_i with the outer cylinder at rest ($\Omega_o = 0$), the CC flow is stable as long as the rotation speed is below Ω_c^0. This was the problem studied by Couette (1890) as a means of measuring viscosity by making measurements of torque exerted by the fluid on the cylinders.

Following from Chandrasekhar (1961), the most general form of the fluid angular velocity $\Omega(r)$ is, for an infinite cylinder,

$$\Omega(r) = A + \frac{B}{r^2}. \tag{1.1}$$

At the boundaries, r_i and r_o,the no-slip condition requires

$$\Omega_i = A + \frac{B}{r_i^2}$$
$$\Omega_o = A + \frac{B}{r_o^2} = 0.$$

Solving for A and B gives

$$A = -\Omega_i \frac{\eta^2}{1-\eta^2}$$
$$B = \Omega_i \frac{r_i^2}{1-\eta^2}$$

where $\eta = r_i / r_o$ is the radius ratio.

This profile is shown below in figure 1.1. is

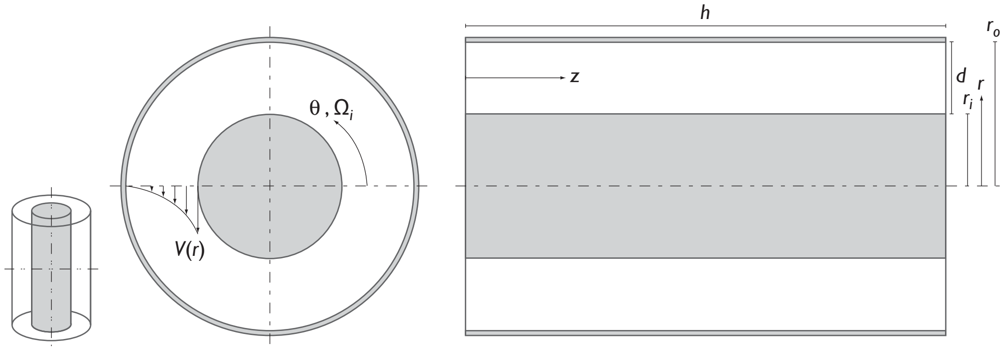

Figure 1.1. Problem geometry in steady case, showing velocity profile of subcritical flow.

Since the fluid at the inner cylinder is in motion while the fluid at the outer cylinder is at rest, a radial pressure gradient is created that increases monotonically outwards. The force created by the pressure gradient is opposed by the spinning of the fluid, which creates a centrifugal force pushing outwards. As long as the centrifugal force is less than the pressure force, then the Couette flow is stable. This condition, in the absence of viscosity, is given by Rayleigh's criterion,

$$\frac{d}{dr}(r^2\Omega) > 0, \tag{1.2}$$

which effectively says that a stratification of angular momentum ($r^2\Omega^2$) about an axis is stable if and only if it increases monotonically outward (Lord Rayleigh 1920). The result of this condition is that, for Couette flow to be stable, the outer cylinder must rotate at a speed greater than η^2-times that of the inner cylinder and in the same sense, i.e. ,

$$\mu = \frac{\Omega_o}{\Omega_i} > \eta^2.$$

Clearly, in the case where the outer cylinder is fixed and in the absence of viscosity, the flow is unstable for any rotation of the inner cylinder.

Couette (1890) noted a sharp increase in torque when the cylinder is rotated faster than a certain rate, but did not offer an explanation as to the cause. Many years later, Taylor (1923) studied the viscous stability problem both theoretically and experimentally, determining both the criterion for stability and the dynamic behavior of the instability. He found that above a critical rotation rate the axial symmetry of the flow is broken and an axially periodic pattern emerges. Although he considered combinations of inner cylinder and outer cylinder rotations, only the case where the inner cylinder rotates while the outer cylinder is fixed is considered further.

In the presence of viscosity, (1.2) is a necessary but not sufficient condition for flow stability. For viscous fluids, Taylor (1923) determined the criterion for stability in terms of the Taylor number. When the outer cylinder is fixed, the Taylor number is proportional to the square of the Reynold's number,

$$Re = \frac{\Omega_i d r_i}{\nu}.$$

For simplicity, the latter is used. It suffices to say that, for $\eta = 0.5$, the critical Reynolds number is $Re_c^0 = 68.19$, where the superscript 0 indicates steady rotation and the subscript c indicates criticality in the limit of infinitely long cylinders.

For $Re^0 < Re_c^0$, the only possible solution is the CC basic state. At Re_c^0, the axial translation symmetry

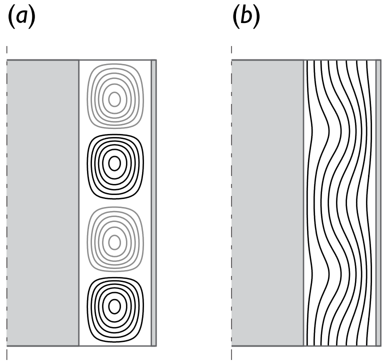

FIGURE 1.2. (*a*) Streamlines and (*b*) angular moment countours of Taylor-Vortex flow just above Re_c^0.

is broken and CC becomes unstable to a periodic pattern of wavelength λ_c, which is nondimensionalized as the wavenumber $k_c = 2\pi/\lambda_c$. For $\eta = 0.5$, the critical wavenumber is $k_c = 3.12$, which corresponds to vortices that have an approximately square crossection. This new stable state, called Taylor-vortex (TV) flow consists of pairs of counter-rotating, toroidal vortices. Streamlines of the pattern and angular momentum contours are shown in figure 1.2.

As the Reynolds number is increased further, the basic state CC is unstable to all periodic patterns whose wavenumber satisfies $(k - k_c)^2 < Re^0/Re_c^0 - 1$, shown by the solid line in figure 1.3 (adapted from Tuckerman & Barkley 1990). Eckhaus (1965) showed that these periodic solutions are also unstable unless their wavenumber falls in the range $(k - k_c)^2 < (Re^0/Re_c^0 - 1)/3$, shown as the dashed line in the figure. This is known as the third-order theoretical Eckhaus band; the actual Eckhaus band is generally more restrictive in fully nonlinear problems like the Taylor-Couette system.

Theoretically, the stable wavenumbers are continuous and bounded by the Eckhaus limit. In the typical Taylor-Couette experiment, the ends are rigid plates or ramps that quantize the stable wavenumbers, allowing only a discrete set of values. This happens because there needs to be an integer number of vortices in the apparatus. This is not the case when the top boundary is the less common free-slip boundary, which supports the continuous Eckhaus band (Tuckerman & Barkley 1990).

The effect of the Eckhaus instability can be clearly observed by forcing the system into an unstable wavenumber. For example, one could obtain a stable flow at $Re > Re_c$ with a particular $k_p \neq k_c$. If Re is decreased until k_p lies outside the stable Eckhaus band, vortex pairs will be created or destroyed in order to adjust the flow to a stable wavenumber. Eventually, an infinite system with a stable flow will

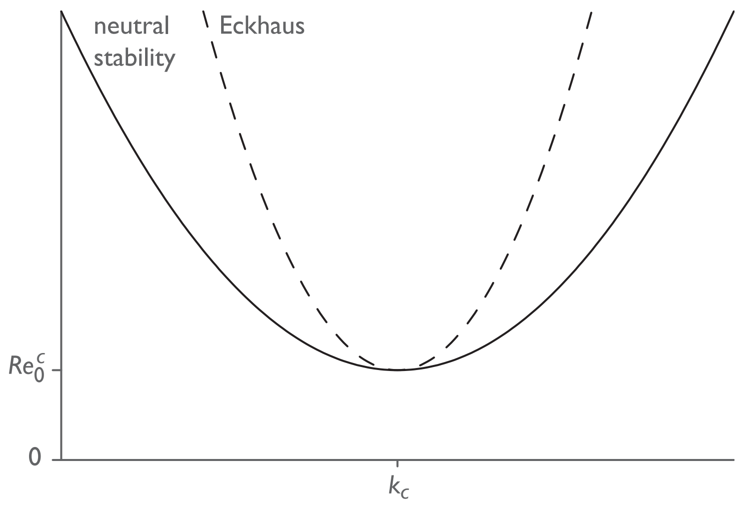

FIGURE 1.3. Wave number dependence on *Re* and the Eckhaus instability.

settle on a uniform wavenumber. A notable exception to resolving the instability by vortex creation or destruction is that under certain boundary conditions (such as the spatially-ramped flow of Ning, Ahlers & Cannell 1990) it is possible for the boundaries to supply a traveling vortex wave that stabilizes an Eckhaus-unstable wavenumber. Since the vortex structure is a repeating pattern, the traveling wave has a characteristic frequency f.

Transitions to other stable states occur at higher reynolds number, but are not considered here. Coles (1965) presents experimental results that document a number of the myriad states.

1.2. Modulated Taylor-Couette flow

In the regime of modulated Taylor-Couette flow considered, the inner-cylinder angular frequency is harmonically modulated in time. The experiments of Donnelly (1964) instigated interest in modulated Taylor-Couette flows. He focused on the case were the rotation is modulated about a nonzero mean with an amplitude that is small compared to the mean rotation. Donnelly found that the onset of the primary bifurcation to Taylor-vortex flow can be delayed to high rotation rates in this manner, i.e. modulation stabilizes the flow.

Soon after Donnelly published his results, theory showed that time-modulation does in fact destablize the flow. This fundamental discrepency between theory and experiments is resolved by reconsidering the criterion for stability, as discussed by Donnelly (1990). In the 1964 experiments, Donnelly ramped the velocity of the inner cylinder in time. He observed what he considered to be a secondary, low amplitude flow just before Re_c^0 followed by a switch to Landau-law dependence of u_r on the mean rotation angular velocity. He considered the latter flow to signal the onset of the instability, but it is more appropriate to consider the first departure from cc to indicate the onset.

After establishing that modulation does in fact destablize the flow, new disagreement between theory and experiments arose with respect to the magnitude of the destabilization and the existence of two stable modes in the zero-mean case came into question.

Weak destabilization was found by Hall (1975), who performed a perturbation analysis that found a small degree of destabilization in limit where the gap between the cylinders is very small in comparison to the radius of the outer cylinder, i.e. $\eta \rightarrow 1$. Riley & Laurence (1976) confirmed these results using Floquet theory. In the zero-mean case, they identified the existence of two stable supercritical modes, one that occurs at relatively lower frequency and another that occurs at higher frequency. Using a Galerkin expansion, they characterized the supercritical behavior of both modes and identified them as synchronous, having a period equal to the that of the forcing. In addition, unpublished experiments by Ahlers (reported by Barenghi & Jones 1989) supported the weak destabilization found by these theories.

Favoring strong destablization were experimental results by Thompson (1968) and by Walsh & Donnelly (1988). Carmi & Tustaniwskyj (1981) extended theoretical consideration of the problem to finite-gap geometry using Floquet analysis and characterized the flow field. At higher frequencies, they achieved qualitative agreement with the stability measurements of Thompson, finding a large degree of destabilization. They did not detect the existence of two stable modes—finding only the mode that Riley & Laurence (1976) identified at higher frequency. They attributed the discrepancy in part to inclusion of specific terms in their approximation that were considered negligible by Riley & Laurence.

Using an amplitude model developed by Hall (1983), Barenghi & Jones computed additional results, addressing the myriad issues of disagreement in the previous results, and introduced basic consideration of noise effects. First, they determined that the time steps taken in the low-frequency computations of Carmi & Tustaniwskyj (1981) were too large to accurately reproduce the exponential decay of the behavior when $Re < Re_c^0$. Second, they compared their results with experiments including those of Donnelly (1964) and Thompson (1968) and Ahlers' unpublished results. By considering the sources of error in the various experiments and the problems in the computations of Carmi & Tustaniwskyj (1981), they concluded that the large degree of destabilization observed in some experiments is due to experimental imperfections. Barenghi & Jones did not find existence of the two competing modes, however. They considered their results on a log scale, which didn't include enough points in the low-frequency range to establish a discontinuity where the mode that is first to bifurcate changes.

1.2.1. *Stable modes in zero-mean modulated flow*

In the zero-mean case, the Reynolds number is a function of time:

$$Re(t) = Re_a \sin(\omega t).$$

The basic state is now the modulated circular Couette (MCC) flow, which has an azimuthal velocity profile that varies in time. Youd, Willis & Barenghi (2003; 2005) used nonlinear computations to reconsider the stability of MCC flow and identified two stable modes, which they termed "reversing" and "nonreversing" Taylor-Couette flow and presented the results of nonlinear computations to characterize the two modes. Again, good agreement is obtained with the results of Riley and Laurence. For reasons that will be explained shortly, reversing flow is here referred to as mode A and nonreversing flow as mode B.

The question that arises from Youd *et al.* (2003; 2005) is whether or not A is due to (1) finite-amplitude perturbations or (2) a linear instability. If (1) is the case, then the narrow-gap approximation of Riley & Laurence is inappropriate. Conversely, the approximation is appropriate if (2) is the case. Avila, Belisle, Lopez, Marques & Saric (2007) performed Floquet to consider this question. The results verify the stability of the MCC flow and nonlinear computations further characterizing the mode competition between the two modes.Figure 1.4 shows the results of the Floquet analysis for the transition from the basic state, MCC flow, to modes A and B. The two curves correspond to the neutral stability curves of the two modes, which are distinguished by their different symmetries.

There are four basic regions in figure 1.4, identified by the flow states which are possible in that region. In the lowermost region, only MCC flow exists and is stable. There are two regions where either A or B exist and an overlap region where both modes exist and are stable. The point $(Re_{a,c}, \omega) = (3.936, 119.4)$ is the bicritical point where both modes bifurcate simultaneously from MCC.

Avila *et al.* (2007) delineated the behavior in overlap region, shown in figure 1.5. At low frequency mode A is the first mode to bifurcate while at higher frequency mode B is the first to bifurcate. There is an overlap region, where both mode A and B are found by nonlinear computations to be stable. The

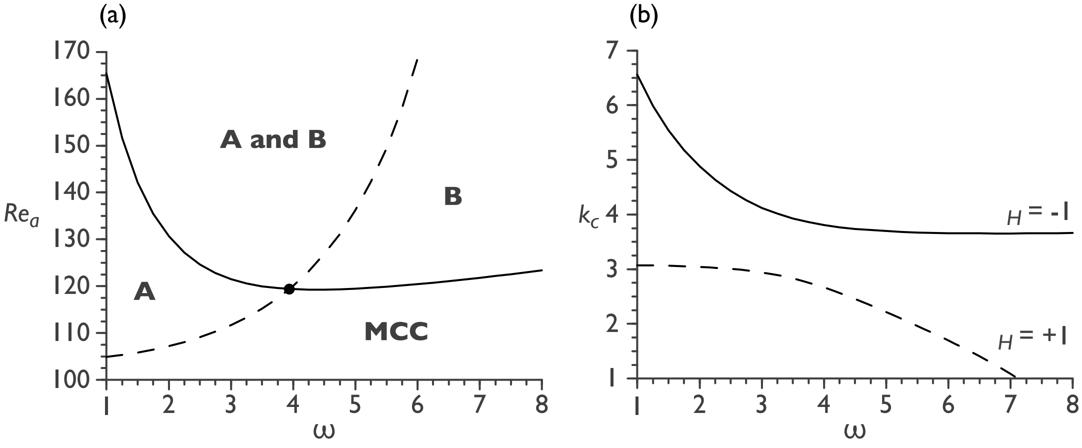

FIGURE 1.4. Results of Floquet analysis from Avila *et al.* (2007). The solid circle denotes the bicritical point $(\omega, Re_{a,c}) = (3.936, 119.4)$.

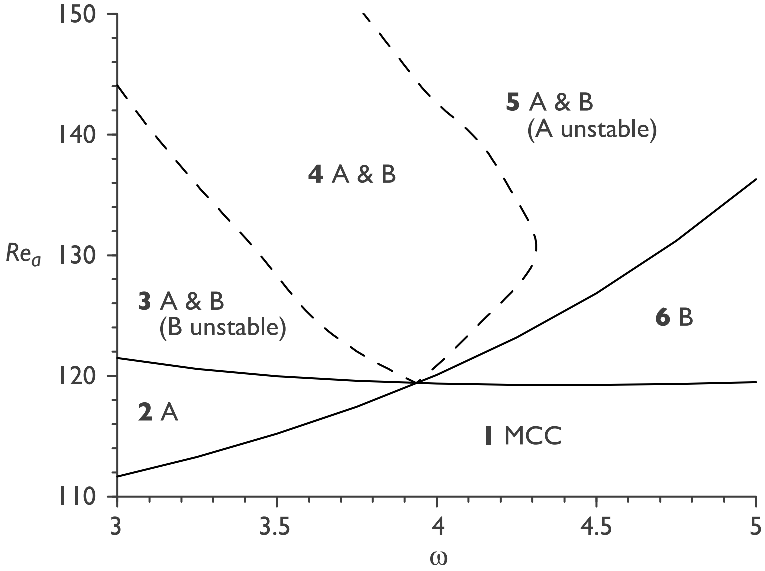

FIGURE 1.5. Stability regions for stable modes. Solid lines are from Floquet analysis above; dashed lines are from nonlinear computations (from Avila *et al.* 2007).

mode selected is dependent on the initial conditions, e.g. if a stable mode A is obtained in region 2, and the frequency is changed to lie within region 4, then the flow will remain as mode A. A mixed mode AB exists in region 4, but is unstable.

The simpler of the two modes is mode B. Figure 1.6 shows contours of the angular momentum rv_θ and azimuthal vorticity ω_θ of this mode. These contours are obtained after the initial transients have decayed, (typically after 10 modulation periods).

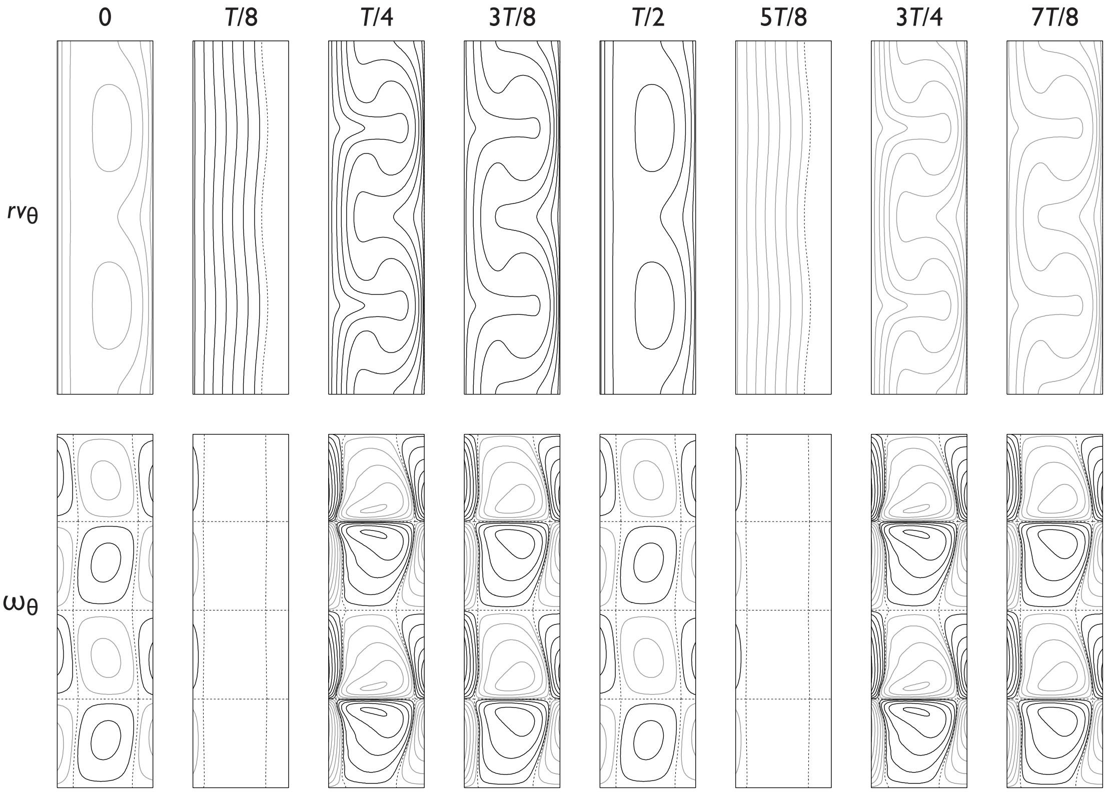

Figure 1.6. Angular momentum (rv_θ) and azimuthal vorticity (ω_θ) contours of mode B (from Avila *et al.* 2007).

At $t = 0$ the amplitude of the modulation is zero and a weak vortex pair from the previous modulation cycle is present. At $t = T/8$, the angular momentum is nearly uniform since vortices have decayed to a small amplitude. At $t = T/4$, the modulation is at a maximum in the positive sense and the vortices are at a maximum as well. In the next few intervals, the cells decay until at $t = 5T/8$, the vortices are at a minimum again. Since the symmetry in this plane is preserved for mode B, the behavior in the second half of the period is the same as that of the first half of the period. The overall half-period symmetry of the mode is preserved: if v_θ pulses in positive θ direction in the first half-period, then it will pulse in the negative direction, with precisely the same amplitude, during the second half-period.

Contours of the same quantities are presented in figure 1.7 for mode A. Mode A differs in two important regards from mode B. First, the overall phase of the behavior is shifted forward in time by $T/8$, that is to say that the amplitude of the vortices in mode A are at a minimum at $t = 0$, versus mode B where the minimum occurs at $t = T/8$. Second, the pattern is shifted by one-half of a wavelength in the axial direction during the later half of the period.

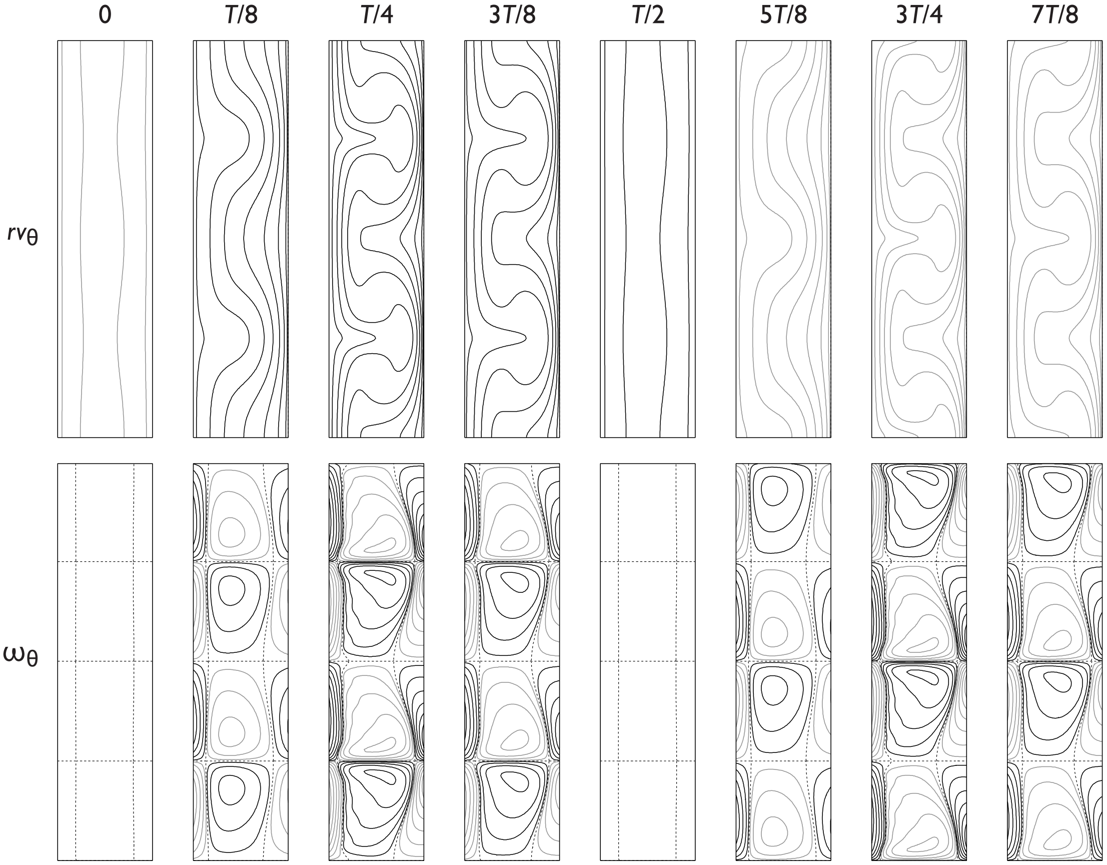

FIGURE 1.7. Angular momentum (rv_θ) and azimuthal vorticity (ω_θ) contours of mode A (from Avila *et al.* 2007).

Thus, both modes are synchronous with the period of the forcing and the difference between the two modes can be explained in terms of their space-time symmetries. This is the issue that arises when terming the two flows "reversing" and "nonreversing." The names are perhaps logical when considering only the radial and axial velocities. But they are misnomers when considering all aspects of the flow, and especially so when considering that the behavior in mode A is an axial shift, not a reversal. It is simpler and more accurate, therefore, to refer to the modes as two different bifurcations A and B from the same basic state.

1.3. Experimental considerations

It is typically the case in Taylor-Couette experiments that every feasible measure to mitigate or eliminate sources of noise is taken. Regardless of the measures taken, a variety of sources of noise are unavoidable. This noise can have a notable impact on the stability of a flow. In low-frequency modulated case, the effects of noise are pronounced because perturbations have a long time to grow and decay in a cycle.

The choice of the appropriate time scale has attracted much attention in Taylor-Couette research. In numerical computations with an infinite cylinder, there is only a single time scale at work: d^2/ν, the viscous diffusion time across the gap. In the finite-length experiments, some processes operate on this time scale in addition to two other time scales: the viscous diffusion time across the length h^2/ν (e.g. Snyder 1969) and a mixed time-scale hd/ν as found empirically by Park, Crawford & Donnelly (1981) and verified numerically by Czarny & Lueptow (2007). There is considerable disagreement in the literature regarding which if any single time scale is most appropriate for the finite-length Taylor-Couette.

In the zero mean case, both Donnelly (1964) and Thompson (1968) observed that "transient vortices" appear whenever the amplitude of the modulation Re_a is greater than Re_c^0. The name transient is a slightly misleading because it arises not because the vortices do decay as $t \longrightarrow \infty$, as one might expect, but because the vortices grow from unavoidable imperfections in the experiments and decay during each period. The vortices are only present when $|Re(t)| > Re_c^0$.

There is a growth phase when $(Re_a - Re_c^0 > Re_c^0)$ that is by an often longer phase of exponential decay when $(Re_a - Re_c^0 < Re_c^0)$. The length of the decay phase is inversely proportion to frequency. At lower frequencies, the energy in the computations is reduced to low levels that are not physically achievable. These levels are below the minimum level of "background" noise. The transient vortices grow from the background noise—which is in experiments is inevitably greater than the exponentially small energy in the numerics. Barenghi & Jones (1989) addressed the issue of background noise by introducing a constant parameter into the amplitude equation derived by Hall (1975). This parameter was chosen to be constant under the reasoning that the noise effects, such as convection, vary on a large time scale. This approach has little physical meaning, but significantly improves the agreement between theory and experiments.

CHAPTER 2

EXPERIMENTAL APPARATUS

The apparatus, shown in figures 2.1 and 2.2, is a reassembly of the original apparatus used by Takeuchi & Jankowski (1981) for the study of spiral Poiseuille flow and later by Cooper, Jankowski, Neitzel & Squire (1985) for temporally-ramped flow. Details of its original construction may be found in Takeuchi (1979). It has been thoroughly overhauled with a new drive system, piping system, and digital-image acquisition system. The scale of the apparatus is uniquely large with the intent to minimize end effects and—although not important in this case—allow a fully-developed axial flow.

The inner cylinder is a stainless-steel pump shaft having a radius of $r_i = 25.4 \pm 0.01$ mm. Three precision-bored, borosilicate glass tube sections form the outer cylinder, each with a constant inner diameter of $r_o = 50.80 \pm 0.05$ mm and nominal length 720 mm. The design radius ratio is thus $\eta = r_i/r_o = 0.500 \pm 0.002$. The length of the outer cylinder is length $h = 2.93 \pm 0.01$ m, which corresponds to an aspect ratio of $\Gamma = 115 \pm 1$. There are four bearings along the length of the test section, each having six degrees of freedom for alignment. The inlet plenum and inner-cylinder bearing house are traverse mounted and it is possible to disconnect the outer cylinder at any of the bearing locations. In this manner, the annulus can be accessed for run-out determination without affecting the alignment. The entire test section is environmentally sealed to minimize the effect of undesirable temperature gradients.

The inner and outer cylinders are rotated independently by Industrial Devices Corporation (IDC) P21V stepper motors having 200 steps per motor revolution. MCG E9 optical rotary encoders, with a resolution of 2000 tics per motor revolution, measure position. A finite-difference approximation is employed to obtained the instantaneous Reynold's number from the position date. The stepper motor connects to a Bayside PX60-10 10:1 gearbox which in turn connects via a timing belt to the inner and outer cylinders. The total gear ratios of the inner and outer cylinders are 200:7 and 240:7, respectively. The motors are controlled by IDC SmartStep23 microstepping integrated controllers, capable of 36000 microsteps per motor revolution. The minimum and maximum rotation rates are 2.00×10^{-4} Hz and 70 Hz. The acceleration range is 0.0015 to 31000 Hz/s.

Because the apparatus was originally designed for experiments involving axial flow, the ends of the test section are not rigid plates or ramps as commonly found in Taylor-Couette experiments. At the lower end of the test section is a step change to an annulus of $\eta < 0.5$. This boundary is more stable than the test section, and thus suppresses vortex propagation (Cooper *et al.* 1985). At the top of the test section is

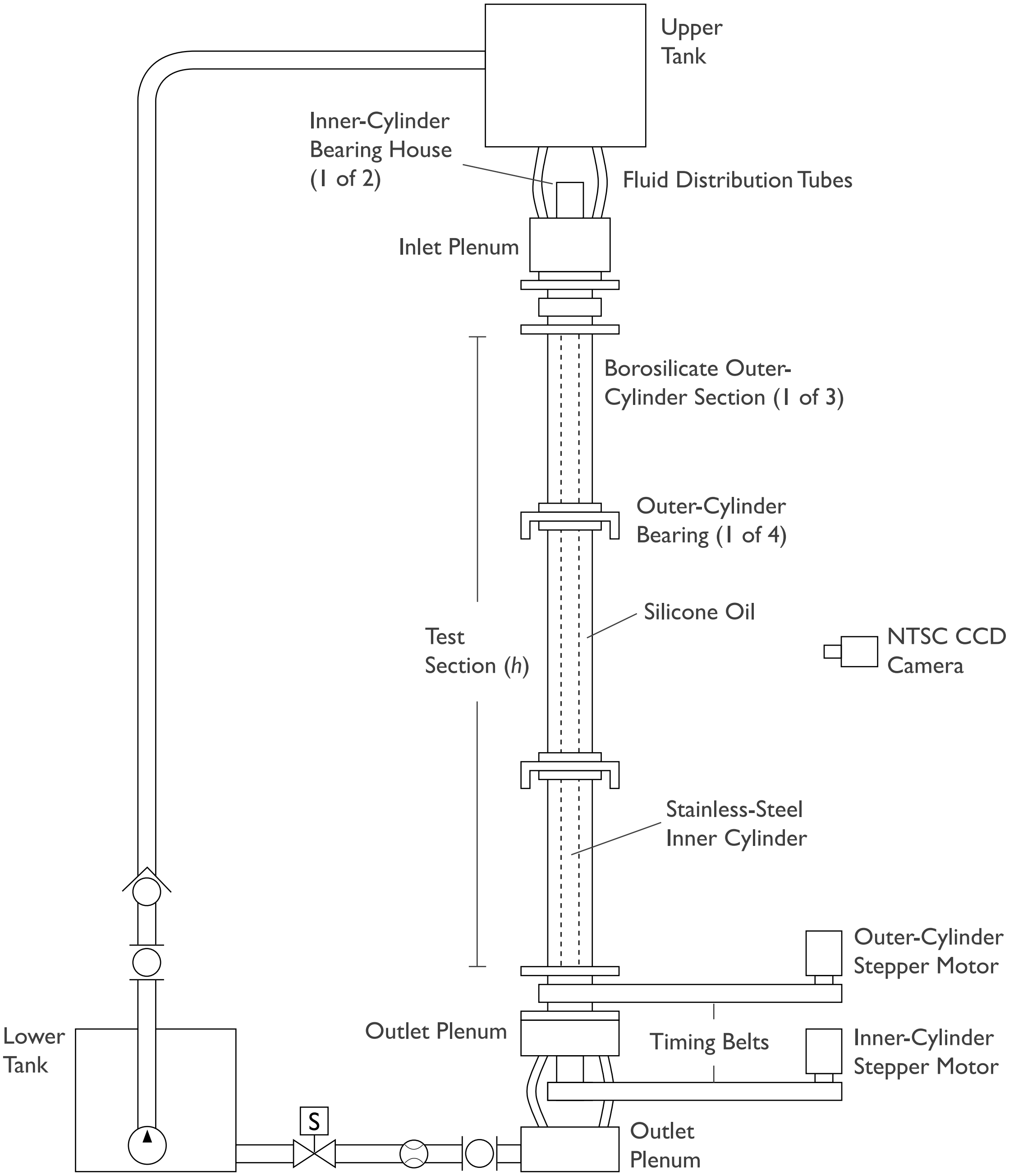
Upper
Tank
Inner-Cylinder
Bearing House
(1 of 2)
Fluid Distribution Tubes
Inlet Plenum
Borosilicate Outer-
Cylinder Section (1 of 3)
Outer-Cylinder
Bearing (1 of 4)
Silicone Oil
Test
Section (h)
NTSC CCD
Camera
Stainless-Steel
Inner Cylinder
Outer-Cylinder
Stepper Motor
Lower
Tank
Outlet Plenum
Timing Belts
Inner-Cylinder
Stepper Motor
S
Outlet
Plenum

Figure 2.1. Diagram of experimental apparatus.

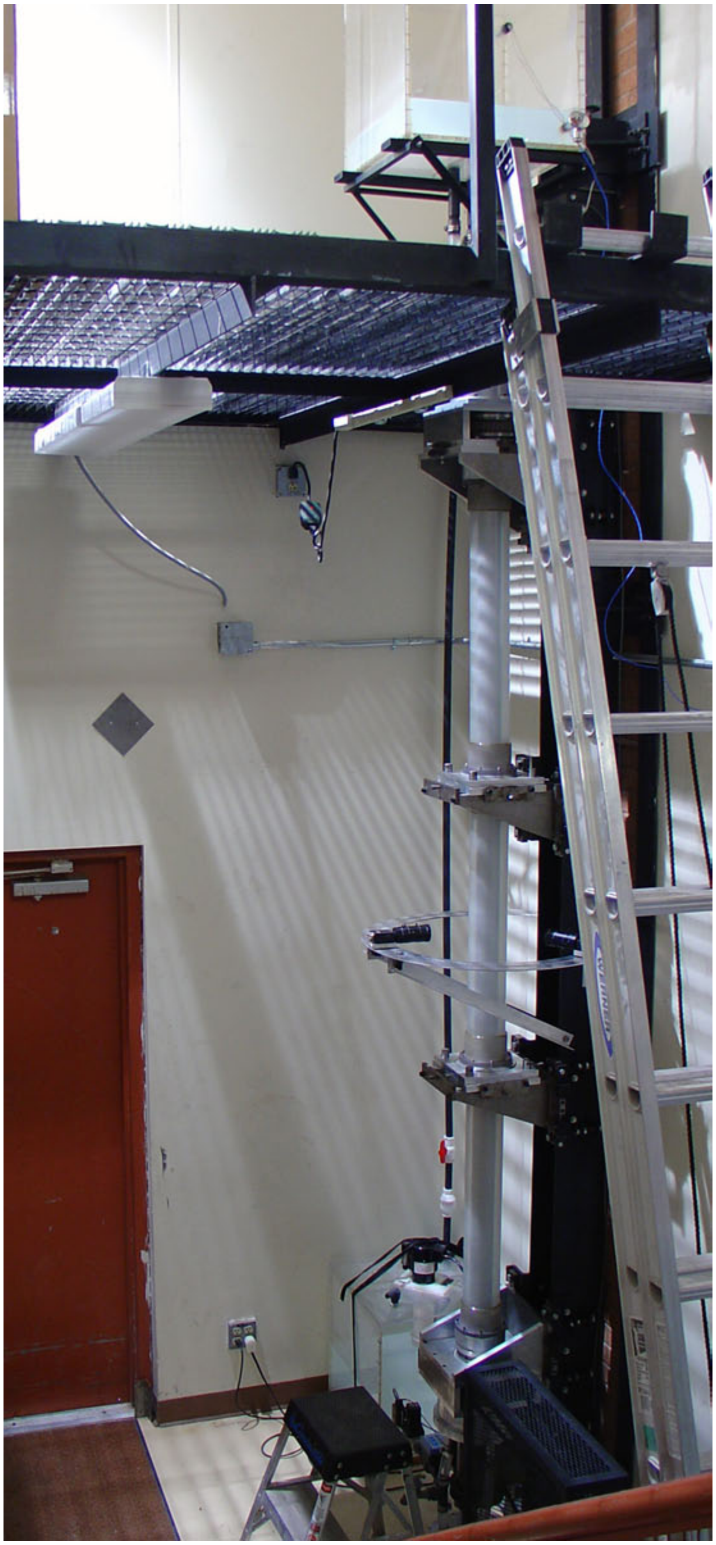

Figure 2.2. Photo of experimental apparatus.

a fixed-area inlet. Experiments were performed with fluid in this inlet and hence the boundary behaves like a free-slip surface. Here, vortices may be created or destroyed as necessary based on the test-section state.

The experimental fluid is 10 cSt (nominal) Dow Corning 200 Polydimethylsiloxane (PDMS) with Flamenco Superpearl 120C+ (mica-TiO_2) flakes used for visualization. Durosense Type T thermocouples are used to monitor the temperature in the upper and lower reservoirs, while resistence-temperature detection (RTD) probes measure the temperature inside the test section chamber and in the room. The thermocouples connect to a National Instruments PCI-6035E 12-bit, 200 kHz data acquisition (DAQ) card through a National Instruments SC-2345 signal conditioning unit. The RTD probes connect to a Hanyoung NX-9 process controller with 4-20 mA output that is connected to the DAQ card. The temperature inside the chamber is typically between the temperature in the upper and lower reservoirs and is used as a measure of the experimental fluid viscosity.

Fluid is pumped from the lower reservoir to the head tank using a Pacer OL50 vertical centrifugal pump at a flow rate of 250 liters per minute (LPM). Axial flow is gravity-driven from the head tank and regulated by a Bürkert Type 1094 proportional valve and measured by a Bürkert Type 8025 inline flow transmitter and Bürkert Type 6223 flow sensor. The minimum measurable flow rate is 5.1 ± 0.1 LPM, which corresponds to an axial flow velocity of 0.014 m/s ($Re \approx 380$) in the test section. The maximum flow rate is 38 ± 1 LPM or 0.1 m/s ($Re \approx 2640$). Although this axial flow capability is not used in these experiments, it was used to cycle the fluid between runs to minimize any axial temperature gradients, clear remnants of vortices from preceding runs, and uniformly distribute the flakes.

A Sony XC-ST50 Monochrome charge-coupled device (CCD) video camera with a Computar MP-1214 monofocal lens is used for image acquisition. The lens has a focal length of 12 mm and is configured such that the viewable length is 610 ± 10 mm, a maximum based on the length of one test section. The camera is connected to a Linux Media Labs LMLBT44 capture card with 640 pixels wide by 480 high. The card is capable of sampling 4 channels simultaneously at a rate of 29.997 Hz.

The results of various measures taken to verify the operation of the apparatus are presented in Appendix A.

CHAPTER 3

EXPERIMENTAL METHOD

The aspects of the experimental method can be group into three basic categories: motion control, data acquisition, and image acquisition. A single C-language program performs all three operations.

3.1. Motion control

The computer sends commands in the IDeal programming language to the motor controller using the RS-232 protocol. The controller operates the stepper motor using in an open loop; the encoder position is read by the computer but not used as a part of the control loop. In fact, this makes sense because the resolution of the encoder (2000 tics/revolution) is less than the resolution of the microstepping controller (36000 tics/revolution).

Velocity commands are sent to the controller by discretizing the zero-mean sine wave. The first step in the discretization is to select the number of points in a period, usually chosen to be 66 points. Since the acceleration and velocity of the stepper motor are specified as integer values—acceleration in the range 1–30 $\times 10^6$ step/s^2 in increments of 1 and velocity in 0–1 $\times 10^6$ step/s in increments of 24—it is necessary to chose the spacing of the points to minimize errors from resolution. This could happen, for example, if the sine wave was discretized using an extremely high number of points per period such that small velocity change has a high error introduced by the rounding to the nearest integer value.

The spacing of the time increments needs to be larger near the peaks of the sine wave (when the acceleration is small) and can be smaller when the acceleration is large while the velocity is near zero. Using the Chebyshev nodes in each half period accomplishes this goal as long as $N/2$ is odd:

$$t_p = \begin{cases} T\{\cos[\pi(N-2p+1)/N]+1\}/4 & 1 \le p \le N/2 \\ t_{p-N/2} + T/2 & N/2+1 \le p \le N \end{cases} . \tag{3.1}$$

The sine wave for one period of the forcing is then generated simply:

$$\Omega(t_p) = \sin(\omega t_p) \qquad 1 \le p \le N.$$

Since the controller can only preform trapezoidal move profiles, the acceleration between two points is

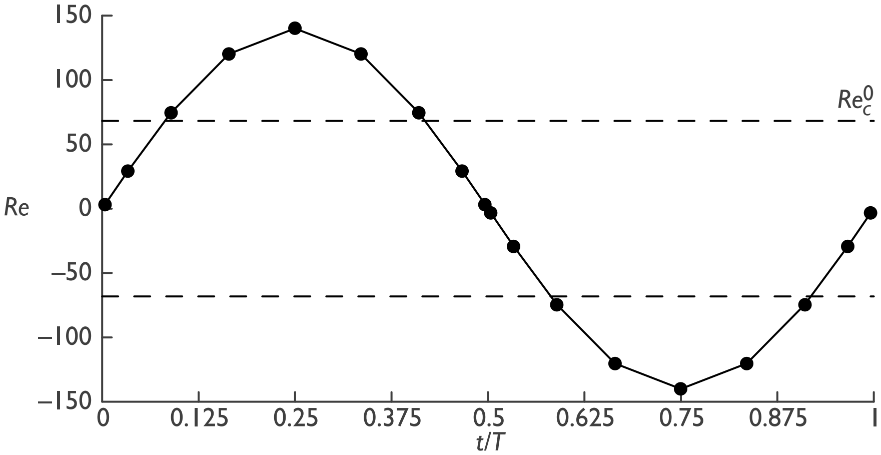

FIGURE 3.1. Discretized sine wave used in motion control.

simply the slope of the line connecting the two points:

$$\alpha = \frac{\Omega(t_{p+1}) - \Omega(t_p)}{t_{p+1} - t_p}$$

An example with 18 points is shown in Figure 3.1.

The C-program measures the temperature and uses the temperature-viscosity regression (see §A.2) to determine the velocities over the course of one period for a given Re_a. These commands are assembled into a loop and sent as a program to the controller in the IDeal language. Most runs consider developing a stable flow at one (Re, ω) and then changing the to another parameter point. This is done by instantaneously changing the frequency and amplitude between forcing periods. There is no communication during a run between the computer and the controller, so all decisions must be made at the start of the run.

3.2. Data acquisition

Measurements of temperature are made at the start of the run and position and temperature measurements are recorded simultaneously with each image. The initial temperature is used to determine the viscosity for control purposes and motion while temperature data acquired during the course of the run are primarily for verification purposes.

3.2.1. *Motion*

The position of the cylinder is measured by an optical rotary encoder with a resolution of 2000 tics per revolution of the motor shaft. With a gear ratio of 200:7 for the inner cylinder, this corresponds to approximately 57140 tics/revolution of the cylinder. An optical encoder outputs two step signals, that are 90° out-of-phase. If the first channel leads the second channel, for example, then the counter knows that the motor is rotating in the positive direction. During each encoder cycle, the signals of the two channels will rise and fall 4 times. A quadrature clock converter is used to count each time the signal rises or falls. The clock converter quadruples the measurable resolution, bringing the motor and inner cylinder resolution to 8000 and 228570 tics/revolution, respectively. The clock converter is connected to a counter on the DAQ board, which is read each time (along with the temperature) in conjunction with each image acquisition. In practice, the encoder used counts only about 99% of the theoretical maximum, with a slight bias in the positive direction (see §A.3).

3.2.2. *Temperature*

The temperature is measured in four places: inside the upper and lower tanks, inside the test chamber, and just outside the test chamber. The typical variation of these temperatures over the course of a run is detailed in §A.2. The initial temperature inside the test chamber is used as an estimate of the experimental viscosity. The temperature data acquired during the run can be used to determine the actual Re and ω at a particular point in time. However, this is not typically done because the measurements are not generally concerned with stability boundary determination and the changes are relatively small (within 1–2%).

3.3. Image acquisition

Space-time images are obtained by observing an axial cross-section of the flow. A camera is oriented such that typically 24 Taylor cells are visible in an image, which is the maximum attainable over the length of one glass section. The technique, illustrated in figure 3.2, follows that of Linek & Ahlers (1998) and countless other papers.

3.3.1. *Visualization using reflective flakes*

Reflective flakes are used as the visualization medium, which tend to align themselves with stream surfaces while their finite thickness causes them to periodically undergo rapid turnover . The behavior of reflective flakes was considered theoretically by Savaş (1985) and compared to experiments. There are two measurements to consider over the length of the frame: the mean and standard deviation of the reflected intensities.

Each time a flake turns over, a spike in reflected light intensity is observed. When the flakes are subject to steady or slowly varying conditions—for example a steady or modulated Couette flow—then

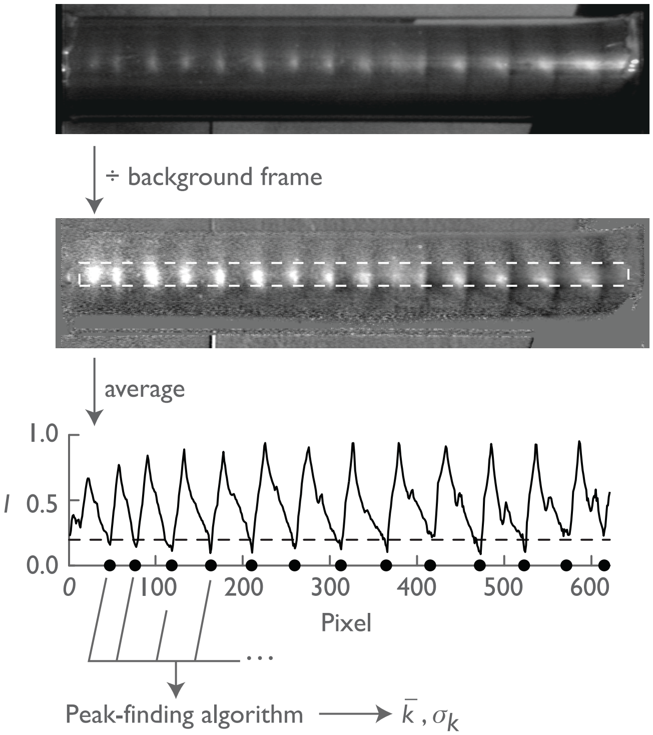

FIGURE 3.2. Image post-processing flow chart.

the reflected light intensity is nearly constant. The rate at which the flakes turn over is proportional to square of the velocity, or the kinetic energy, which means that mean intensity will increase with increasing energy.

When the flakes observe rapidly changing conditions such as a sudden ramp in velocity they will re-orientate to the new conditions. When this reorientation happens, the reflected light intensity will peak to a well-defined maximum value and then settle on a new, steady value. The realignment is essentially a random process, so the standard deviation will spike as well.

In the case of a more complicated flow such as a Taylor-vortex flow, the reflected light intensity will vary over the extent of the vortex cell as the flakes cycle through the cell, continuously realigning with the streamlines as they circulate. The presence of a cell thus increases the standard deviation of reflected intensities. This is often used to determine the onset of the Taylor-vortex flow instability, (e.g. Weisberg *et al.* 1997).

Once the instability sets in, the standard deviation of reflected light will increase with increasing energy because the flakes will realign more rapidly as they cycle through a cell, resulting in greater variation from the mean alignment. This rate of increase proportional to energy will level off as the flakes achieve the maximum intensity. The mean intensity is proportional to the energy in the cell, again since the flakes turn over more rapidly as they rotate faster.

In this manner, the mean and standard deviation can be used as a measure of the flow energy. In an unsteady flow with large variations, however, it can be difficult to decouple the effects above to determine which factor is influencing the mean or standard deviation. Furthermore, nonuniform lighting can impart biases in the measurements that are not easily quantified. Because the problem under study is indeed unsteady, statistical calculations on the light intensity are used qualitatively.

3.3.2. *Construction of space-time diagrams*

Space-time diagrams offer a wealth of information about the spatiotemporal behavior of the flow. Before starting a run, a series of background images are acquired with the inner cylinder stationary. The apparatus is then operated at a specified Re_a and ω and image data are collected at a frequency of about 1 Hz throughout the run.

The intensities in the time history frame (a) are divided by the corresponding intensities of the background image (i.e. a value of 1 in the result indicates that the intensity of the pixel is unchanged from that of the background image). A slice is taken from the center of the resultant image (b), spanning the usable height of the frame and averaged over 15 pixels (typically) in the azimuthal direction. These slices are assembled into a time history, rescaled based on the minimum and maximum values, and then normalized using an adaptive histogram filter.

3.3.3. *Determination of the wavenumber*

The wavenumber is determined by finding distances between the local minima intensities of an axial slice. The pixel intensities of a particular slice (c) are low-pass filtered and a peak-finding algorithm locates the peaks by finding where the finite-difference of the intensity crosses zero, neglecting any peaks that are closer than physically meaningful or are above a certain threshold (typically $I = 0.2$). These peaks correspond to the inflow jets (the thin, dark structures). The peak selected in the dark region varies by at most ± 2 pixels for a constant Re flow. The mean wavenumber $\bar{k}$ and standard deviation σ_k for the slice are then determined using the measured dimension of a pixel (d).

3.3.4. *Determination of traveling wave frequency*

Cross-correlation is employed to determine the frequency f of traveling waves having similar dynamics to that observed by Ning *et al.* (1990). This is performed quite simply by selecting a reference slice at the start of a space-time diagram and then computing the correlation coefficient of the rest of the history image with respect to the reference slice. In the presence of the traveling wave, the correlation coefficient is periodic, with a slow decay due to sensor noise and other factors. A Blackman filter is applied to the signal and then the discrete Fast-Fourier Transform is taken, using the peak as the frequency of the traveling wave.

CHAPTER 4

RESULTS AND DISCUSSION

4.1. Transition to to mode B

The first result considered is the transition from the modulated Circular Couette flow to mode B. The case $\omega = 6.1$ is considered as an illustration of the typical behavior on this apparatus.

Figure 4.1(*a*) shows the basic state at Re_a well below critical $Re_{a,c} \approx 120$, which is here characterized by transient vortices. This is as expected from previous results by Thompson (1968) and Walsh & Donnelly (1988). The relatively small amplitude of these vortices is demonstrated by the blurry appearance of the image that results from a small difference in light intensity between the background and the experimental image. Spikes in intensity, illustrated in Figure 4.1(*b*) are observed to occur at two times: the first corresponds to maximum positive velocity and the second corresponds to maximum acceleration α. Spikes at the corresponding negative peaks should also be expected, but do not appear here. It is believed that the flakes align optimally with the light source in the positive direction. Thus when the velocity is negative, a consequence of the small amplitude of the transient vortices is that the energy change is not enough to register under the present lighting conditions.

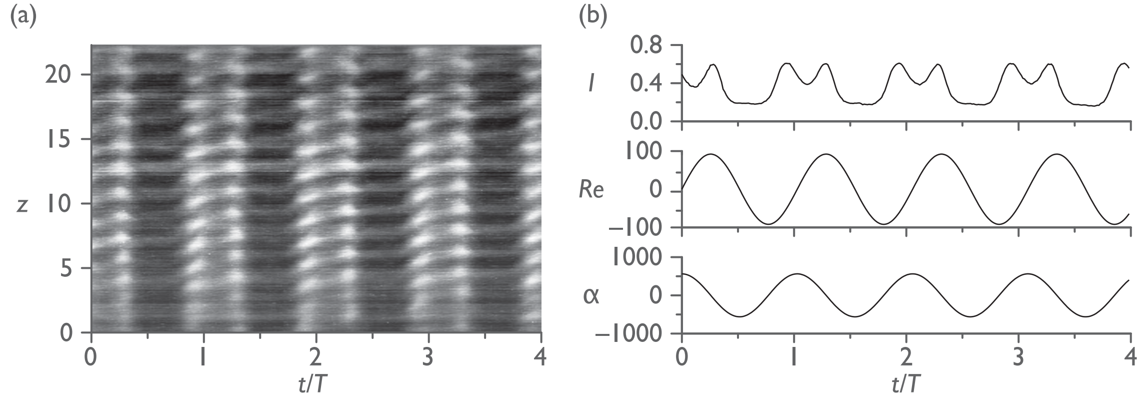

FIGURE 4.1. (*a*) Time history at $Re_a = 92$, $\omega = 6.1$ showing subcritical vortex structure that grows and decays in each period. (*b*) standard deviation compared to Reynolds number and angular acceleration.

Around $Re_a = 120$, a front is observed to move into the center test section. This front is a traveling wave of supercritical vortices propagating from the free-slip boundary at the top of the apparatus, apparently supplying energy to the transient vortices in the lower part of the apparatus. A time history on a much longer time scale in figure 4.2 shows the front clearly at $z \approx 17$. Above $z \approx 17$, the flow is considered to be mode B based on the wave number of $k \approx 3.4$. There is an apparent overlap region for

$z \in [9, 17]$, and noise amplified vortices below $z \approx 9$. The vortices in the lower region have an unsteady wave number.

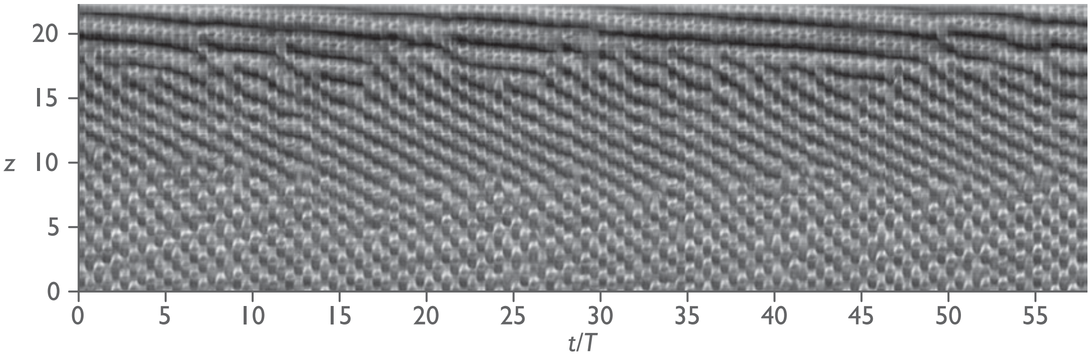

FIGURE 4.2. Time history at $Re_a = 120$, $\omega = 6.1$ showing front between noise-sustained vortices below $z \approx 17$ and mode B above.

As Re_a is further increased, this front moves further in the negative z-direction. Around $Re_a = 140$ (figure 4.3), the front is no longer in the center section. At this point, it is possible to consider the frequency f of the traveling wave, plotted in figure 4.4, which decreases with increasing *Re*. These frequencies are comparable in magnitude the frequencies observed by Ning *et al.* (1990) for vortices induced by a spatial ramp in the test section.

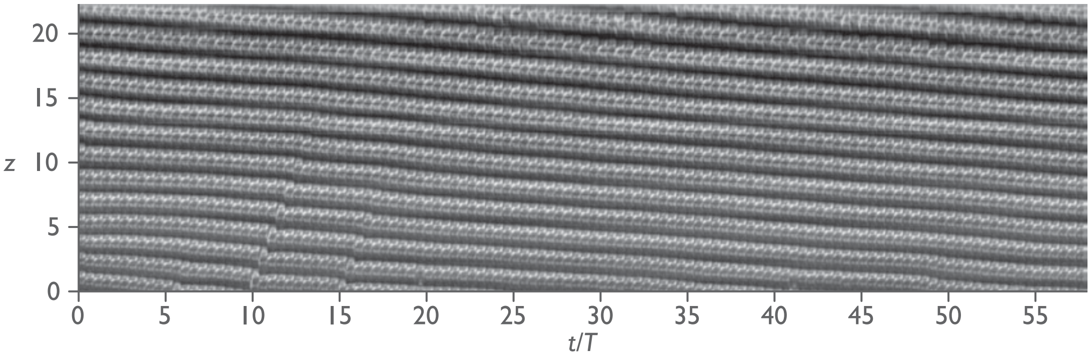

FIGURE 4.3. Time history at $Re_a = 140$, $\omega = 6.1$, showing a traveling wave with frequency $f \approx 0.06$.

Around $Re_a = 200, f$ is over 100 and can be neglected: the time scale of the wave is much greater than the observed time scale of the dynamics of modes A and B (see §4.3). It is in this range that the primary results of this thesis are obtained.

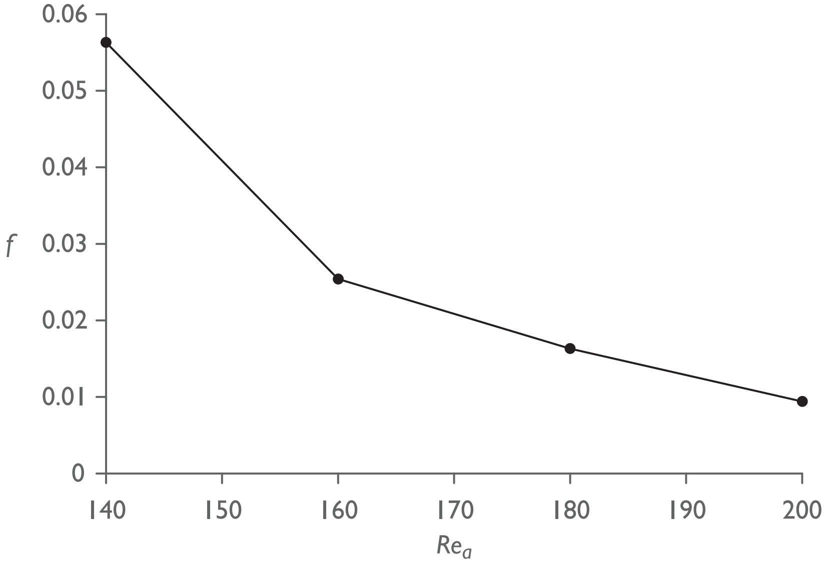

FIGURE 4.4. Frequency of traveling wave versus *Re* for $\omega = 6$.

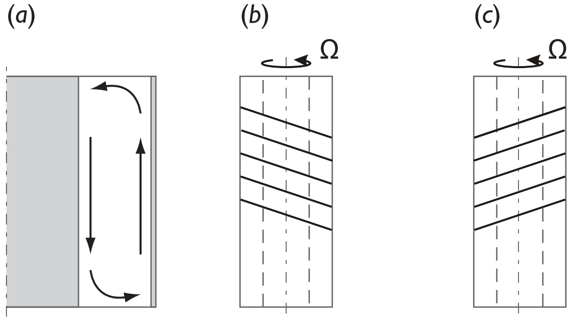

FIGURE 4.5. (*a*) Direction of fluid motion for stationary cylinders subject to a postive radial temperature gradient; (*b*) leftward spiral; and (*c*) rightward spiral (adapted from Deters & Egbers 2005).

4.2. Temperature dependence

In agreement with experimental results by Deters & Egbers (2005), a radial temperature gradient has significant impacts on the flow dynamics. If the cylinders are stationary, a positive radial temperature gradient (for example if the temperature in the room is increasing with time) is observed to induce circulation over the length of the apparatus, shown qualitatively in figure 4.5(*a*). The fluid moves upward close to the outer cylinder and return back down the inner cylinder. When the cylinders are rotated, inducing a spiral vortex state, as shown in (*b*) (*c*), is induced. This spiral is analogous to that of spiral Poiseuille flow.

Because the forcing is about a zero mean, this spiral is allowed to propagate into modes A and B when

$|Re| < Re_{a,c}$. The direction of the spiral can be observed to depend on the sign of the radial temperature gradient in figure 4.6. When the radial gradient is positive and the forcing velocity is small, the spiral is apparent as a rightward spiral. Conversely, a negative gradient induces a leftward spiral, demonstrated by the change in direction triggered by turning on the air conditioning at $t/T = 6$.

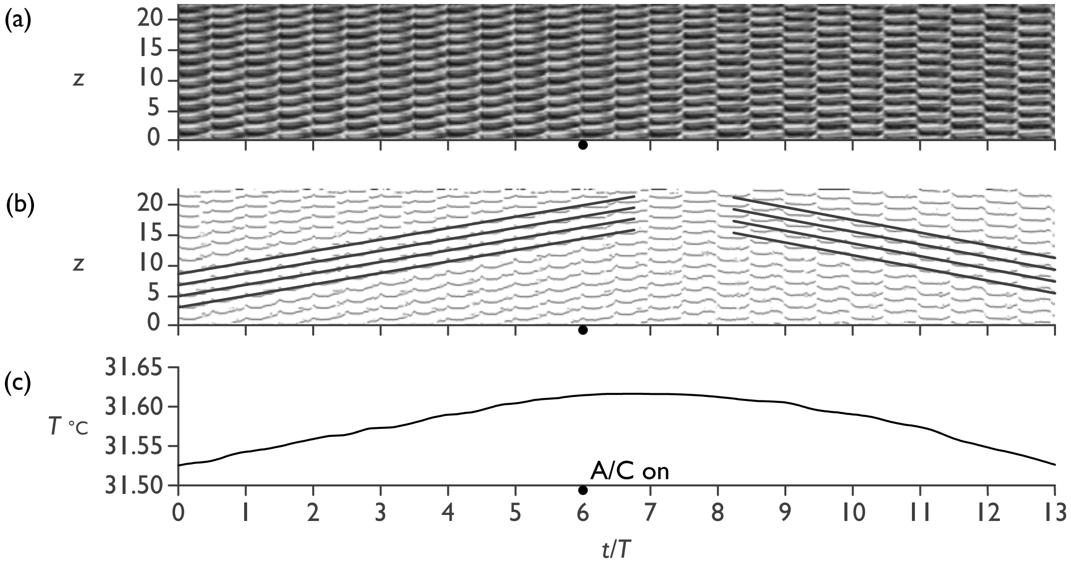

FIGURE 4.6. Data at $Re_a = 120$, $\omega = 2.5$ showing the change in behavior with the sign of the radial temperature gradient: (*a*) time history; (*b*) highlighted inflow jets and markings to illustrate spiral direction; *b* temperature of air inside test section chamber.

A second effect of the radial temperature gradient is to trigger an entirely new wavenumber in the flow. At $Re_a = 240$ and $\omega = 1$, the wavenumber is expected to be in the range $k \in [2.6, 3.3]$. This is the result as expected in figure 4.7(*a*). In (*b*) of the same figure, the effect of the radial gradient is pronounced, selecting a wavenumber that would otherwise be unstable. The qualitative behavior is still that of mode A as explained in the following section.

4.3. Modes A & B

Figure 4.8 shows a representative example of (*a*) stable mode A and (*b*) stable mode B. By all of the available measurements—and notwithstanding the small traveling wave noted above–the dynamic behavior of the two modes is as expected from the numerics. This can most readily be seen by the defining characteristics of the flow: the behavior of the dark inflow jets. In (*b*), the jets are observed to remain fixed in the axial direction which contrasts with the shift of $\lambda/2$ observed in (*a*). The measured wavenumbers agree well with the numerics.

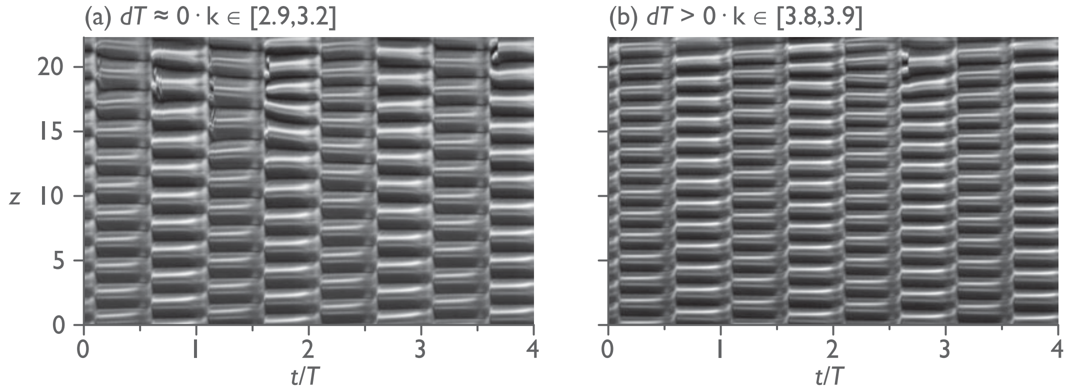

FIGURE 4.7. Data at $Re_a = 240$, $\omega = 1.0$ showing the change in behavior with the sign of the radial temperature gradient: (*a*) $dT \approx 0$, $k \in 2.8$; (*b*) $dT > 0$, $k \in 3.8$.

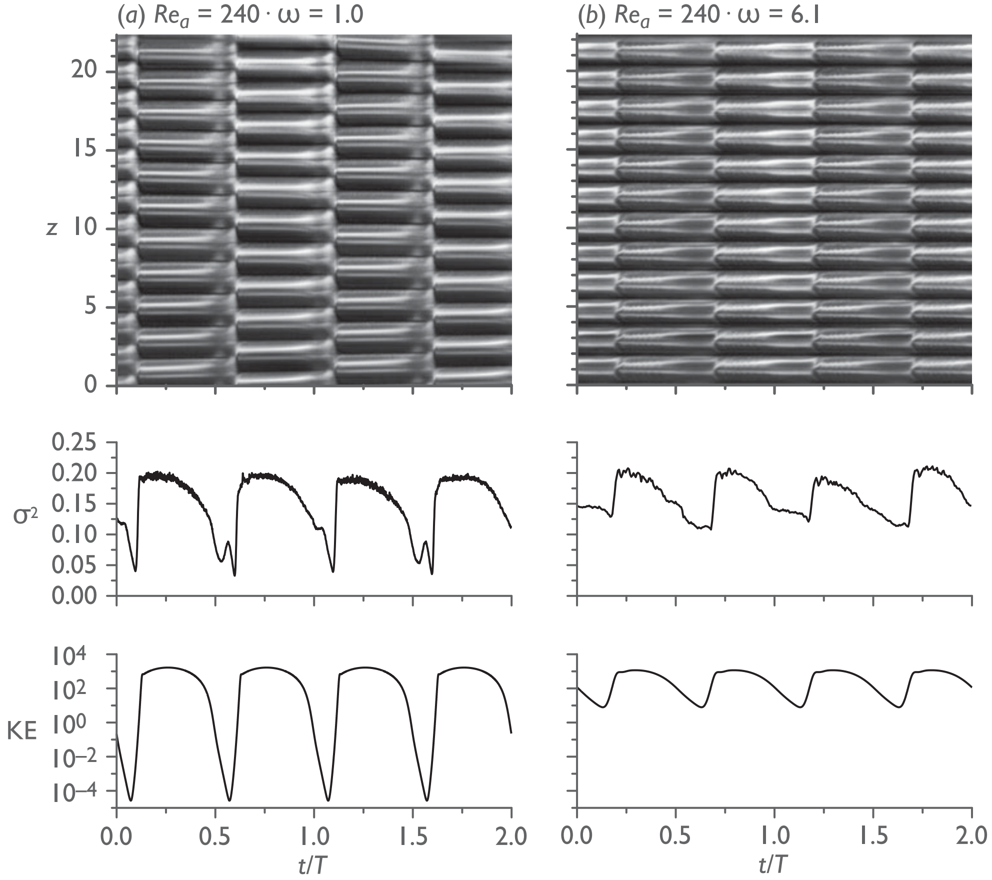

FIGURE 4.8. Space-time diagrams, normalized standard deviation σ^2, and kinetic energy KE at $Re_a = 240$: (*a*) mode A at $\omega = 1.0$, $k = 3.0$ and (*b*) mode B at $\omega = 6.1$, $k = 3.4$.

The agreement between the energy as indicated by the standard deviation in reflected intensity and the kinetic energy (KE) in the numerical results is excellent as well, but some justification of this assertion is necessary. Each half period is characterized by alternating intensities: e.g. during $t/T \in [0.125, 0.625]$ the intensity appears dimmer than $t/T \in [0.625, 1.125]$. Both the mean intensity and standard deviation show periodic step changes between these intervals, which correspond to the instants that the numerics predict a reversing pulse in the azimuthal velocity. Since the light is off-center and nonuniform, the step change is attributable to a rapid realignment of the flakes and not a substantive change in the energy of the flow. Hence, the standard deviation is arbitrarily scaled here by the mean squared intensity, which mitigates the impact from nonuniform lighting.

The minimum level of decay is related to the frequency of the forcing and does not define a distinction between modes A and B. When $Re(t)$ is $|Re < Re_c^0$, the flow undergoes a period of exponential decay, which has a pronounced effect at low frequencies. At higher frequency, the period of exponential decay is shorter and the energy does not fall as low. This is likely because the decay rate is independent of frequency.

Of note is the small spike in (*a*) just before the energy rises again, which is not present in the theoretical energy data. This spike occurs at the same time and with the same amplitude as the pulse synchronous with the acceleration in figure 4.1(*b*). A similar (though fainter) pulse is also observed at $t/T = 0.5$, with further supports the assertion that nonuniformities in lighting prevented the negative pulse from appearing in figure 4.1.

4.4. Transition from one mode to the other

The empirical data at $Re_a = 240$ suggest that the two modes compete within a region bounded by $\omega \in [1.5, 2.5]$. The observed wavenumbers of all runs at $Re_a = 240$ are presented in figure 4.9.

The criteria for stability here are that the flow has settled on a wavenumber that is constant within the experimental uncertainty in k, ± 0.1. The flows presented in §4.3 fulfill this criterion. They correspond to ω far from the bound of coexistence region predicted by the numerics to be at $\omega \in [1.6, 2.2]$.

Far away from the competition region, the flow is stable and settles on a wavenumber in the expected range for mode A at lower Re_a and mode B at higher Re_a. When close to the competition region, e.g. $\omega = 1$, occasionally the flow would experience difficulty in settling on a stable wavenumber.

The dashed lines and triangles represent unsteady behavior. This is a consistent behavior in the range

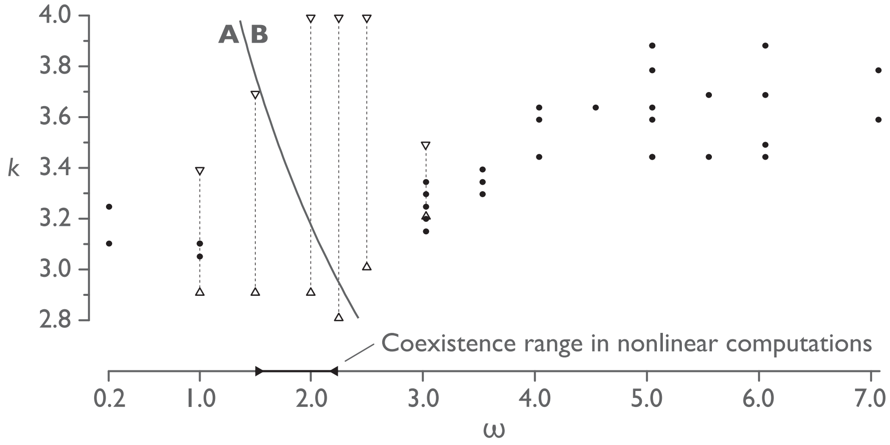

FIGURE 4.9. Diagram of observed behaviors at $Re = 240$. ● corresponds to observed stable wave numbers, while ▽ and △ respectively represent the overall maxima and minima of unsteady wavenumbers over all runs. The range of the coexistence region as computed by the nonlinear computations (Avila *et al.* 2007) is shown on the abscissa.

$\omega \in [1.5, 2.5]$. For these frequencies k varies within k_{min} to k_{max}. The range of k does not necessary cover this entire range, as enumerated for each observation in figure 4.10. The sawtooth behavior can be seen in figure 4.11

This variation is often sawtooth-like as seen between approximately $t/T = 3$ and $t/T = 8$ in the previous figure. When the wavenumber varies in this manner, k nominally decreases until it suddenly increases. This behavior may be due to Eckhaus, which inevitably leads to creation or destruction of a vortex pair if the wave number is outside of the stable band. When a vortex pair is created, the flow adjusts to the new wave number for the number of vortices in the test section. The creation or destruction is sudden, which leads to a step change in the wave number. So, in the case where the k is decreasing, a vortex pair will be created whenever k leaves the stable Eckhaus band.

Although the sawtooth appearance is not by any means the typical behavior of the unstable wavenumber, it is the most the distinctive feature that appears. The absence of sawtooth-like variation suggests that the new wave number is more susceptible to another instability or the noise than it is to Eckhaus. The noise is important here because a stable k is only stable for small perturbations. If a perturbation is sufficiently large, then it can trip a transition to a different k. As the condition approach the competition region, the magnitude of the disturbance needed to render the flow unstable decreases until it's quite possible that it is below the level of the noise. This results in a constantly varying wave

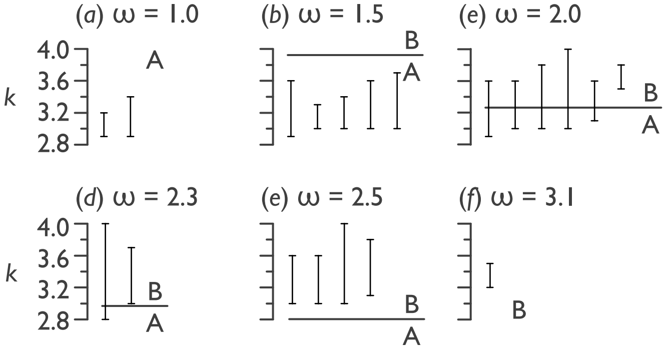

FIGURE 4.10. Observed ranges of unsteady wave numbers in the competition region.

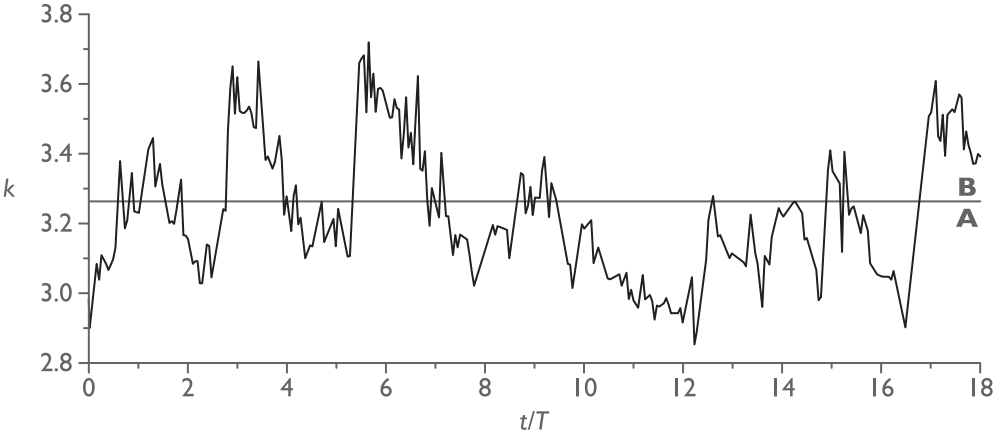

FIGURE 4.11. Typical wave number variation for $Re_a = 240$, $\omega = 2.0$.

number that due to the nature of noise is not deterministic even though trends are sometimes observed for short periods of time.

4.5. Time scales

In studying competition between the two modes, the shortcomings of the present apparatus for considering this problem become vividly clear. Issues with temperature were resolved by enclosing the apparatus, the influence of the traveling wave at low Re_a was mitigated by focusing on $Re_a > 200$, and the dynamics of the two modes were characterized by focusing on ω far from the competition region.

But, as attempts were made to study behavior within the competition region, the data were complicated by the influence of two time scales on which different aspects of the flow operate: d^2/ν and hd/ν. There is no evidence of any development occurring on the h^2/ν time scale because it is impossible in the current installation to perform a run on the order of 240 hours in length. Figure 4.12 shows a representative example of the two time scales, which was acquired starting from rest. The qualitative

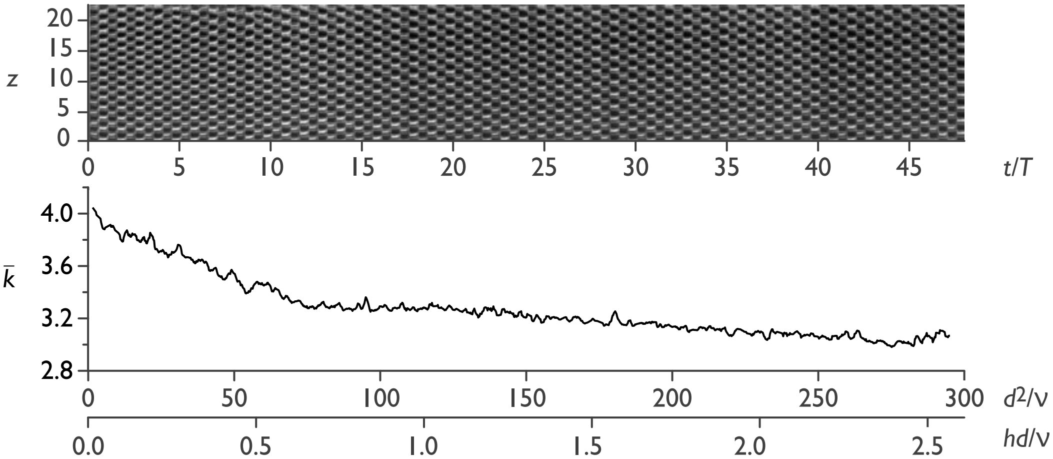

FIGURE 4.12. Representative example of a flow settling on a uniform and steady wavenumber. Conditions are $Re = 240$, $\omega = 1.0$.

behavior of the flow is well established with $15d^2/\nu$ and the wave number decreases rapidly until about $75d^2/\nu$. At this point, the wavenumber slowly decreases until $275d^2/\nu$, where the subsequent behavior is uncertain because the flow conditions were naïvely switched to the next point after 48 forcing periods. Thus, this run does not conclusively establish the final wavenumber of the flow. Even so, it's safe to say that it is 3.2 ± 0.1, as there is no evidence of instability and flow was within this range by $100d^2/\nu$.

The transients would almost certainly be sufficiently reduced within $10hd/\nu$ in a manner analogous to the typical $10d^2/\nu$ that is observed in the nonlinear computations. Even when operating far from the competition region, the flow still typically would take a time on the order of hd/ν to settle on a uniform and steady wavenumber—although it is clear which mode is present much sooner than this time.

CHAPTER 5

CONCLUSIONS

Although complications were encountered throughout the course of experimentation, the results are encouraging. Although the data do not directly support coexistence of the two modes, they certainly do not preclude it. There is a very clear region of competition in which no stable flow was attained. This is most likely attributable to noise that, despite the best efforts, was not sufficiently minimized to the extent that the apparatus could be considered "perfect". This is especially evident when considering features such as the traveling wave at low velocity, or the difficulties with convection effects.

The most relevant time scale was found to be at least hd/ν, which is approximately 2 hours with the current configuration. The hot Arizona summer, unfortunately, did not allow runs that lasted more than 10–12 hours, which meant that it was difficult to perform a survey and obtain stable flows within the alloted time for an experiment. This is the reason why the results focus purely on $Re_a = 240$. At this Re_a, the signal-to-noise ratio was sufficiently high that problems with the traveling wave were minimal and stable flows could be obtained outside of the competition region.

Future work on the project should include a complete overhaul of the apparatus or—preferably for the study of this problem—construction of an table-top apparatus with a much smaller viscous time scale. Although the present apparatus may have a future yet in the study of problems related to its original intended purpose (Couette flows with an axial pressure gradient), the impracticality of its size and the challenges in eliminating temperature gradients severely limit the effectiveness of results in modulated flows.

In addition, the tolerances of all aspects of the apparatus are not at the $O(10^{-3}\text{ mm})$ level typical of modern Taylor-Couette experiments. Even with replacement of worn components, the alignment of the three independent outer-cylinder sections is almost certainly impossible to complete within this tolerance range. The expense involved in an overhaul to get the apparatus to this level is comparable to that of constructing a smaller apparatus that is better suited to modulated flows.

Regardless of the tolerances, however, the inclusion of rigid end plates in the test section would likely do a great deal towards addressing the traveling wave issues and time that it takes for the apparatus to settle on a uniform wavenumber. The time scale benefit would result because the end plates discretize the range of stable wave numbers. It is also much simpler to introduce endplates into numerical computations than it is to study a free-slip surface.

The results certainly support the value of reflective flake experiments and have benefited from their economy. Even so, considering this problem using techniques such as Particle-Image Velocimetry (PIV) and/or Laser Doppler Velocimetry would greatly enhance the breadth of data and potential for comparison with the theory. PIV, in particular, would facilitate a direct comparison with flow field parameters of the numerics, e.g. the angular momentum and vorticity of figure 1.6.

The data presented conclusively verify the stability of two stable modes in the zero-mean modulated regime of the Taylor-Couette system. The agreement between the observed wave numbers and the computations is quite good, and the dynamical behavior of each mode is verified using the available experimental methods, most significantly the behavior of the inflow jet in each half period. For all data that demonstrated a stable mode, the behavior of these jets corresponds to the that's expected to be stable in that region according to the nonlinear computations. For parameter values near the competition region as expected from the numerical computations, there is strong evidence of competition between the modes, as the flow is more susceptible to noise than the stable flows observed at conditions far from the region.

Even despite the noise effects, the quality of the agreement between nonlinear computations for a theoretically perfect, infinite cylinder and an finite experimental apparatus with various types of noise and unique boundary conditions is encouraging. Through interaction with computational scientists, the understanding of the behavior observed experiments is much more readily ascertained. Although they approach the solution to the problem with a distinctly different approaches, the experiments and numerics should eventually converge on a single answer when all effects are considered and accounted for. The occasional disagreement between the two essentially incomplete answers to the question that is addressed here usually offers suggestion for either scientist to consider a part of the parameter space in greater detail or try to determine the underlying cause responsible for the discrepancy.

Even though the parameters in the Taylor-Couette problem seems deceptively simply when compared to those of laminar–turbulent transition, the amount of work that remains to be done to improve the correlation between theory and experiments demonstrates the value of considering a simple though related problem as a means to finding and understanding of more complex one.

REFERENCES CITED

Avila, M., Belisle, M. J., Lopez, J. M., Marques, F. & Saric, W. S. 2007 Mode competition in modulated Taylor–Couette flow. *J. Fluid Mech.* In preparation.

Barenghi, C. F. & Jones, C. A. 1989 Modulated Taylor–Couette flow. *J. Fluid Mech.* **208**, 127–160.

Carmi, S. & Tustaniwskyj, J. I. 1981 Stability of modulated finite-gap cylindrical Couette flow: linear theory. *J. Fluid Mech.* **108**, 19–42.

Chandrasekhar, S. 1961 *Hydrodynamic and Hydromagnetic Stability*. London: Oxford University Press.

Coles, D. 1965 Transition in circular Couette flow. *J. Fluid Mech.* **21**, 385–425.

Cooper, E. R., Jankowski, D. F., Neitzel, G. P. & Squire, T. H. 1985 Experiments on the onset of instability in unsteady circular Couette flow. *J. Fluid Mech.* **161**, 97–113.

Couette, M. M. 1890 Etudes sur le frottement des liquids. *Ann. Chim. Phys.* **21**, 433–510.

Czarny, O. & Lueptow, R. 2007 Time scales for transition in Taylor-Couette flow. *Physics of Fluids* **19**.

Deters, T. & Egbers, C. 2005 The Taylor–Couette system with radial temperature gradient. *Journal of Physics: Conference Series* **14**, 138–142, presented at the Fourteenth International Couette Taylor Workshop.

Donnelly, R. J. 1964 Experiments on the stability of viscous flow between rotating cylinders. iii. Enhancement of stability by modulation. *Proc. Roy. Soc. Lond. A* **281**, 130–139.

Donnelly, R. J. 1990 Externally modulated hydrodynamic systems. In *Nonlinear evolution of Spatio-Temporal Structures in Dissipative Continuous systems*, pp. 31–43. New York: Plenum Press.

Eckhaus, W. 1965 *Studies in non-linear stability theory*. New York: Springer-Verlag.

Hall, P. 1975 The stability of unsteady cylinder flows. *J. Fluid Mech.* **67**, 29–63.

Hall, P. 1983 On the nonlinear stability of slowly varying time-dependent viscous flows. *J. Fluid Mech.* **126**, 357–368.

Linek, M. & Ahlers, G. 1998 Boundary limitation of wave numbers in taylor-vortex flow. *Physical Review E* **8** (3), 3168–3174.

Lord Rayleigh 1920 On the dynamics of revolving fluids. *Scientific Papers* **6**, 447–53.

Ning, L., Ahlers, G. & Cannell, D. S. 1990 Wave-number selection and traveling vortex waves in spatially ramped Taylor–Couette flow. *Phys. Rev. Lett.* **64** (11), 1235–1238.

Park, K., Crawford, G. L. & Donnelly, R. J. 1981 Determination of transition in Couette flow in finite geometries. *Phys. Rev. Lett.* **47** (20), 1448–1451.

Riley, P. J. & Laurence, R. L. 1976 Linear stability of modulated circular Couette flow. *J. Fluid Mech.* **75**, 625–646.

Savaş, Ö. 1985 On flow visualization using reflective flakes. *J. Fluid Mech.* **152**, 235–248.

Snyder, H. A. 1969 Wave-number selection at finite amplitude in rotating Couette flow. *Journal of Fluid Mechanics* **35** (02), 273–298.

TAKEUCHI, D. I. 1979 A numerical and experimental investigation of the stability of spiral poiseuille flow. PhD thesis, Arizona State University, Tempe, Arizona.

TAKEUCHI, D. I. & JANKOWSKI, D. F. 1981 A numerical and experimental investigation of the stability of spiral Poiseuille flow. *J. Fluid Mech.* **102**, 101–126.

TAYLOR, G. I. 1923 Stability of a viscous liquid contained between two rotating cylinders. *Phil. Trans. Royal Soc.* **A223**, 289–343.

THOMPSON, R. J. 1968 Instabilities of some time-dependent flows. PhD thesis, Massachusetts Institute of Technology, Cambridge, Massachusetts.

TUCKERMAN, L. S. & BARKLEY, D. 1990 Bifurcation analysis of the Eckhaus instability. *Phys. D* **46**, 57–86.

WALSH, T. J. & DONNELLY, R. J. 1988 Taylor-Couette flow with periodically corotated and counterrotated cylinders. *Phys. Rev. Lett.* **60** (8), 700–703.

WEISBERG, A. Y. 1996 Control of transition in taylor-couette flow with axial modulation of the inner cylinder. PhD thesis, Princton University, Princeton, New Jersey.

WEISBERG, A. Y., KEVREKIDIS, I. G. & SMITS, A. J. 1997 Delaying transition in Taylor–Couette flow with axial motion of the inner cylinder. *J. Fluid Mech.* **348**, 141–151.

YOUD, A. J., WILLIS, A. P. & BARENGHI, C. F. 2003 Reversing and non-reversing modulated Taylor-Couette flow. *J. Fluid Mech.* **487**, 367–376.

YOUD, A. J., WILLIS, A. P. & BARENGHI, C. F. 2005 Non-reversing modulated Taylor-Couette flows. *Fluid Dynam. Res.* **36**, 61–73.

APPENDIX A

APPARATUS VERIFICATION

A.1. Alignment

Each bearing mount on the apparatus has 6 degrees of freedom for alignment. The outer cylinder is traverse mounted and allows disconnection of a glass section at any of the bearings. The cylinders can then be raised and the inner cylinder accessed without affecting the alignment.

The inner cylinder is more or less “aligned by default”. There is a very narrow range of alignment in which the cylinder will rotate freely. This range depends chiefly on the alignment of the outer cylinder: as long as the outer cylinder is aligned and the inner cylinder is concentric within a relatively small range, then the inner cylinder will rotate. It is difficult to quantify the absolute alignment of the inner cylinder since even the order of tightening the bolts could throw it out of alignment.

However, the alignment can be quantified relative to the outer cylinder. For the outer cylinder, each bearing was aligned independently, starting from the bottom. A teflon ring machined to 2.46 cm was used as a guide. The ring was placed on the inner cylinder, and each bearing was adjusted until the space between the ring and the outer cylinder wall was approximately equal around its circumference. This means that the maximum possible misalignment at each bearing is 0.04 cm or 1.6%.

After alignment, run-out of the inner cylinder was measured at each bearing using a dial displacement gauge with resolution of 0.002 cm. It was found to reach a maximum of 0.025 cm (1.0%) at the midsection. Run-out of the outer cylinder was unmeasurable, which is expected since the position of the bearings are immobile after alignment.

Including the dimensional tolerances and the foregoing, the gap width over one glass section is controlled to within 1.9%. Including local deviations near the bearings, the variation in gap width over the entire length is 3.7%.

A.2. Temperature and viscosity

The temperature dependence of the viscosity was measured to within 0.3% using an Ubbelohde viscometer manufactured by Cannon Instrument Company. An exponential regression (with a correlation coefficient of 0.9996) was fitted to the data:

$$\nu(T) = 15.98e^{-0.01849T},$$

valid for $T \in [10, 30]$°C. The propagated uncertainty in viscosity is ± 0.1cSt.

Measurements are made in four locations during a run: inside the upper and lower tanks, in the chamber near the center glass section, and in the room outside the chamber. The difference in temperature between the two reservoirs is nominally 0.5°C. The chamber temperature is typically sinusoidal with an amplitude of 0.1°C about the upper-tank temperature. Since the temperature inside the chamber is the closest measurement to the center glass section—where images are acquired—it is used for the viscosity calculation.

Typical variation over 30 forcing periods at $\omega = 5.1$ is shown in figure A.1 below. The temperature inside the chamber tracks the sinusoidally-varying room temperature with a reduced magnitude of variation. In this case, it is higher than the room temperature, but this is not necessarily the case.

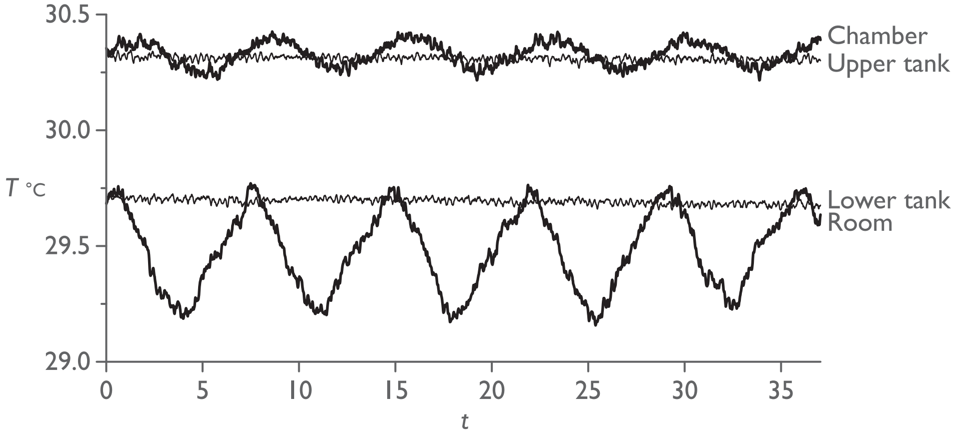

Figure A.1. Typical temperature variation over 30 forcing periods at $\omega = 5.1$.

Since the Prandtl number of PDMS is much higher than air, it is less susceptible to changes in temperature than the surrounding air. Thus, although the variation inside the chamber is nominally ±0.1°C, the actual variation seen by the fluid is even lower.

Including all of the above uncertainties, the instantaneous uncertainty in *Re* and ω are 1.4% and 2.2%, respectively.

A.3. Modulation

The experiments are performed by modulating the velocity of the inner cylinder about a zero mean. The controller that processes commands sent to the stepper motor only has the capability of accepting "trapezoidal" move profiles. This means that the acceleration between any two velocities can only be constant, although there will be some unavoidable ramp up and ramp down.

In order to verify the discretized sine wave as described in §3.1, the encoder position was read by the computer over a series of periods. This was performed with 66 points in a period, which was the typical resolution used throughout the experiments. Re is determined from θ measurements by using the finite centered difference:

$$Re_i = \frac{\theta_{i+1} - \theta_{i-1}}{2(t_{i+1} - t_{i-1})}$$

where i is an index corresponding to a particular point in time. The actual frequency and amplitude were then recovered using nonlinear fitting:

$$Re(t) = A_0 \sin A_1 t + A_2$$

where A_0, A_1, and A_2 are fitting parameters corresponding to Re_a, ω and the phase ϕ, respectively. The correlation coefficient of the fit is nominally 0.9999. ϕ is typically $O(10^4)$ and can safely be neglected.

One regular and predictable error was that the fitted ω obtained was always greater than the commanded frequency. After rounding to nearest tenth using the appropriate significance, this was only significant for $\omega > 3.0$, which added 0.1 to ω (e.g. for $\omega = 3.0, A_1 = 3.1$).

A comparison of the measured velocity and a pure, fitted sine wave is shown in figure A.2. The position is plotted here because the finite differencing to determine Re introduces an error that is on the order of the measured error. There is one other remark to make on this figure, which concerns

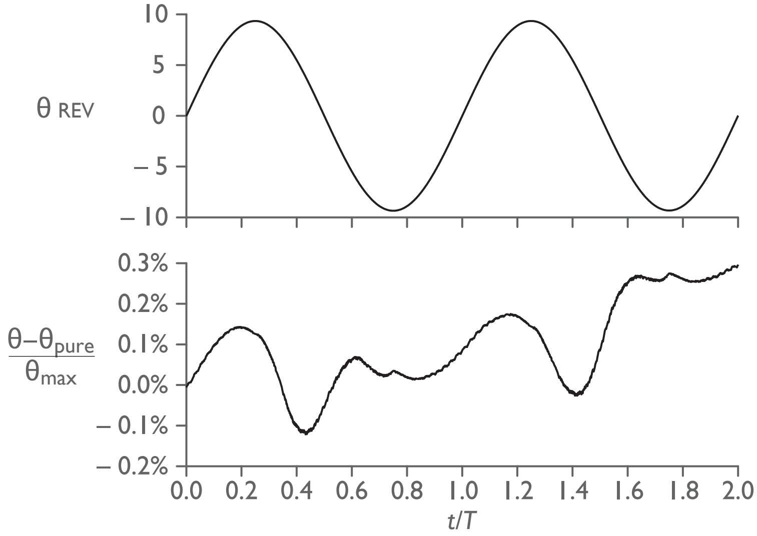

FIGURE A.2. Error in generated sine wave from a pure sine wave as measured by the encoder.

the observed positive drift in the error. This drift is attributable to the encoder, which inconsistently measured between 7800 and 7900 pulses per revolution, biased in the positive direction. The DAQ card does not support Z-indexing, which sets the counter appropriately each time a full revolution is made by the encoder. If this had been the case—which it is when the encoder is connected to the motor controller—there is no bias in one direction or the other. There also was no bias when a different encoder was used, but that unit ceased to function properly.

As explained previously, the encoder is directly connected to the DAQ card in order to record the data on the computer. The drift is barely registrable after taking the finite difference for fitting purposes. Thus, because no other meaningful quantitative measurements are made from the encoder data, the drift is neglected. When ignoring the drift, it can be seen that the error is periodic.

A.4. Critical Reynold's number for the first birfucation in the steady case

The criterion for stability of circular Couette flow in the case of steady rotation is well-known and established. For $\eta = 0.5$, this criterion is that as long as $Re^0 < Re_c^0 = 68.19$, then the Couette flow is stable. Above Re_c^0, the flow bifurcates to Taylor-vortex flow.

A slowly ramped flow is used to determine Re_c. Park *et al.* (1981) empirically determined the ramping rate in order to avoid hysteresis in accelerating or decelerating the flow. They defined a criteria based on a nondimensional acceleration,

$$a = \frac{\delta Re^0}{\delta t^*}\frac{hd}{\nu} < 10$$

where t^* is in seconds. Unfortunately, the minimum acceleration on the present apparatus was found to be $a = 97$. Alternative methods, such the stepping method used by Weisberg (1996) are significantly more complicated and it is only necessary here to get an idea of the Re_c^0, not to establish a definitive value.

Figure A.3 shows a plot of standard deviation of reflected intensity σ_I versus Re^0 for acceleration and deceleration at this rate for $Re^0 \in [10, 87]$. From this plot and the associated time history, it is necessary to decide on a criterion for transition. For reasons due to noise or the non-quasistatic ramping, a non-axisymmetric mode appeared just before the expected axisymmetric Taylor-vortex flow. The expected axisymmetric mode is of interest here and is therefore the criterion used for the determination of Re_c. The non-axisymmetric mode that appears just before onset of the axisymmetric mode is of low amplitude, as σ_I is on the order of the value when no vortices are present. It may well be a small-amplitude modulation effect due to noise from the stepper motor which does. The motor does, impose such a minute modulation on Re_0 because of the discretization inherent in its design.

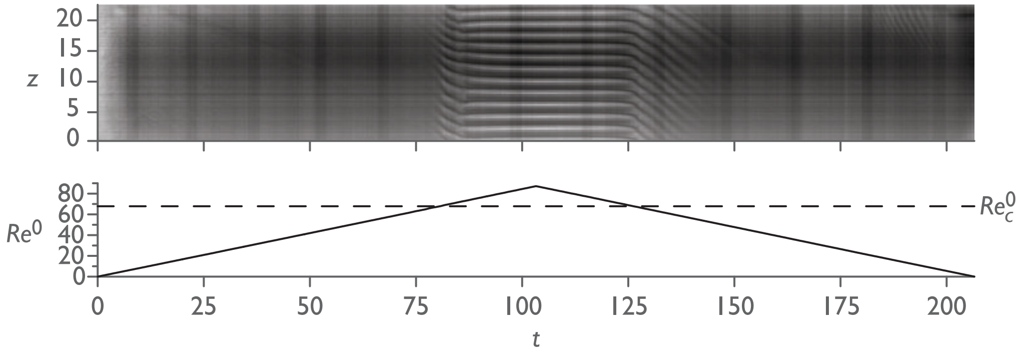

FIGURE A.3. Standard deviation plotted for ramping Re^0 to determine Re_c^0.

Even with this relatively large acceleration by the standards of Park *et al.* (1981), minimal evidence of hysteresis was observed. The results show $Re_c^0 = 68.1$ during ramp up and $Re_c^0 = 71.8$, which corresponds to 5% hysteresis. This compares favorably with the expected value, as $Re_c^0 = 68.19$ is within this range. For simplicity, I take the mean and introduce the appropriate uncertainty, finding $Re_c^0 = 70 \pm 1$.

The data were processed and an average of the measured standard deviation was taken at each point, shown below in figure A.4.

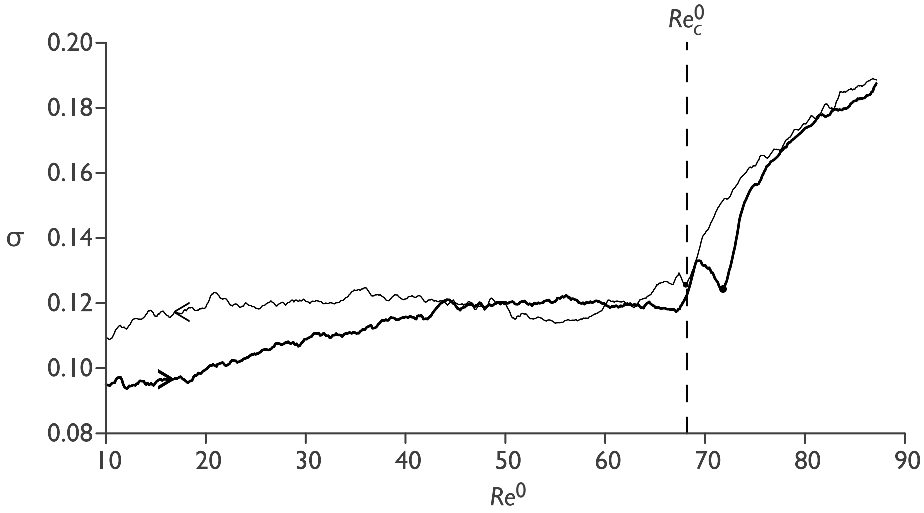

FIGURE A.4. Standard deviation plotted for ramping Re^0 to determine Re_c^0.

A.5. Length measurement

A $24d$ ruler with markings at $1d$ intervals was placed on the surface of the outer cylinder to calibrate the length measurement. The design distortion of 0.3% over the frame was not measurable and the size of a pixel was found to be $0.04d$. The peak finding algorithm considers peaks below a certain threshold, typically $I < 0.4$. When including the width of a peak, the uncertainty in measured wavenumber is ± 0.1.

A.6. Vibration and roughness

The vibration and the roughness of the inner cylinder were also measured and found to be negligible. The roughness was measured using a Mitutoyo Surftest SJ-201P Profilometer and found to be within the dimensional tolerance. PCB 356A32 tri-axial accelerometers measured the vibration on the apparatus during modulated rotation. The vibration in all axes is periodic with an amplitude less than 0.01 m^2/s and a frequency of 200 Hz. The small magnitude of this vibration is expected because vibrations created by the motor (approximately 3 times greater in amplitude) are significantly damped by the usage of a timing belt.